Acoustic Backscatter and Attenuation Due to River Fine Sediments: Experimental Evaluation of Models and Inversion Methods

Adrien Vergne, Céline Berni, Jérôme Le Coz, Florent Tencé

Water Resources Research

RESEARCH ARTICLE

Key Points:
- Acoustic backscatter and attenuation of a homogeneous suspension of fine river sediment were measured in a laboratory tank
- The results of existing models are highly sensitive to particle size distribution uncertainty
- Inversion using both backscatter and attenuation yielded accurate concentration estimates

Correspondence to:
C. Berni,
celine.berni@inrae.fr

Acoustic Backscatter and Attenuation Due To River Fine Sediments: Experimental Evaluation of Models and Inversion Methods

Adrien Vergne[1] , **Céline Berni[1]** , **Jérôme Le Coz[1]** , and **Florent Tencé[1,2]**

[1]INRAE, UR RiverLy, River Hydraulics, Villeurbanne, France, [2]Now at STRATO - LATMOS Laboratoire Atmosphères, Milieux, Observations Spatiales, Paris, France

Abstract The hydroacoustic monitoring of suspended sediment concentration (SSC) in rivers is based on the inversion of backscatter and attenuation models. To evaluate such models, acoustic backscatter and attenuation were measured from a homogeneous suspension of fine river sediments (clay) in a laboratory tank at various concentrations in the range 1–18 g/l. Agreement between the modeled and measured acoustic backscatter and attenuation values was found to be relatively poor. The results are highly sensitive to particle size and shape which come with large measurement uncertainties and they can be significantly improved by adjusting plausible particle parameters. Various inversion methods combining single or multiple frequencies, analysis of backscatter and/or attenuation, spherical or oblate shape hypothesis for particles and fixed or estimated lognormal grain size distribution are tested. The most promising inversion methods using both backscatter and attenuation information led to accurate SSC estimates.

1. Introduction

Following the success of the Acoustic Doppler Current Profiler (ADCP) technology for monitoring river discharge, there has been a growing interest in the last decade in extracting information on Suspended Sediment Concentration (SSC) from acoustic backscatter in rivers. One major advantage of using sonar systems such as ADCPs or Acoustic Backscatter Systems (ABSs) for monitoring SSC in rivers is the capacity of these instruments to provide measurements at a much higher spatial and temporal resolution than traditional water sampling techniques. Despite the efforts recently made to find a relation between SSC and acoustic backscatter in rivers (e.g., Gray & Gartner, 2009; Venditti et al., 2016), most studies remain empirical and site-specific. Such calibrations shift when sediment properties change which requires intensive water sampling to limit the uncertainty in SSC. The development of more general, physically based methods applicable in rivers is needed.

The sonar response of suspended sediments is determined by sound backscattering and sound attenuation. Both processes are strongly determined by the characteristics of the suspended scatterers. Bimodal Particle Size Distributions (PSDs) are commonly observed in rivers (e.g., Agrawal & Hanes, 2015; Armijos et al., 2017). The first mode is usually composed of silt and clay sediment particles that are often fairly homogeneously distributed throughout the river cross-section. We do not expect these particles to gather in large flocs (Burban et al., 1989; Droppo, 2001) as rivers often show low organic matter, no salinity, and relatively high turbulence during high sediment load events such as floods. The impact of flocculation on acoustic backscattering has been studied in other contexts (MacDonald et al., 2013; Rouhnia et al., 2014; Thorne et al., 2014; Vincent & MacDonald, 2015). The second mode is made of fine to coarse sand particles and it usually presents strong lateral and vertical gradients, with concentration increasing towards the bed. Sonar technology could potentially provide information on both of these modes (Thomas & Marino, 2021). Even when the interest is only in monitoring sand SSC, the impact of both fine and coarse suspended sediments on the recorded backscatter signal must be assessed (Vergne et al., 2020).

Thanks to substantial efforts in acoustical oceanography (Hay, 1991; Hay & Sheng, 1992; Moate & Thorne, 2012; Sheng & Hay, 1988; Thorne & Buckingham, 2004; Thorne et al., 1993; Thorne & Meral, 2008), the acoustic response of a suspension of sand particles is now relatively well understood and modeled. Inversion techniques have been developed based on these models, the most powerful ones using multiple sound frequencies and computing both SSC and particle size along the backscatter profile (see Thorne &

Hurther, 2014, for a review). Compared to marine science, the understanding of river suspension backs-cattering is much less advanced (see Szupiany et al., 2019, for the latest significant advances). Deploying ADCPs horizontally in rivers often provides access to a homogeneous suspension of fine sediment along the acoustic beams, which allowed to monitor fine SSC through either empirical approaches (Landers et al., 2016; Moore et al., 2012; Topping & Wright, 2016; Wright et al., 2010) or multifrequency inversion (Moore et al., 2013). Nevertheless, such approach relies on extrapolating literature results on the acoustic response of sand suspension that might not be suitable for river fine sediments (Vergne et al., 2020).

Trying to retrieve suspension characteristics from acoustic measurements using a limited number of sound frequencies is typically an ill-posed inverse problem, even when using simplified acoustic models. Therefore, one usually needs to fix some parameters of the suspension prior to the inversion. The remaining free parameters are then inverted. The applicability of an inversion method in a riverine environment is a trade-off between the required prior information—that can be missing and/or difficult to estimate—and the precision of the inversion outputs. Even when using a calibrated instrument in a fairly well-known suspension with water samples, physically based inversion may fail. The reasons why existing backscatter and attenuation models may produce large errors between observed and modeled SSC are still debated. A serious candidate is the possible inadequacy of commonly used equations to reflect the actual acoustic response of river fine suspended sediments. Indeed, no laboratory experiments in controlled conditions are available in the literature for fine particles representative of river conditions, as opposed to sand particles (see for example Moate & Thorne, 2012). This source of error needs to be isolated from other sources and investigated thoroughly.

The objective of this study is to test the efficiency of existing backscatter and attenuation models for a homogeneous suspension of natural river clay sediment particles in laboratory-controlled conditions. The efficiency of inversion methods designed to retrieve SSC from acoustic signal is also studied in the simplest case of a homogeneous suspension along the acoustic beams. Primary un-flocculated particles were considered. The acoustic backscatter and attenuation at multiple frequencies were measured using a calibrated ABS. The concentration in the laboratory tank was gradually increased in the range ~1–18 g/l. This range of concentrations was chosen as a representative of high to very high SSC observed in rivers. The material and methods for these experiments is presented in Section 2. In Section 3, the data are compared to existing backscatter and attenuation models in order to review the efficiency of these models. Then, in Section 4, four inversion methods, including an original one, are tested, and their outputs are discussed. A discussion on the applicability of existing acoustic models to river suspensions and advices for field applications are provided in Section 5. Conclusions are drawn in Section 6.

2. Material and Methods

We consider here a homogeneous suspension of noncohesive solid particles in a tank. An acoustic system is plunged into water in such a way that it not only emits a sound but also records the sound that is backscattered from the media. Several pulses are emitted and recorded for different suspended sediment concentrations. In this part, we first present the theory related to such a set-up and then present the set-up more in detail.

2.1. Backscatter and Attenuation Models

In the monostatic configuration, when an acoustic transmitter and receiver are actually the same piston transducer, scatterers of random position lead to an echo signal that is described by the sonar equation:

$$\overline{V_{rms}^2} = \frac{16\pi}{3} \frac{k_t^2 s_v}{\psi^2 r^2} e^{-4(\alpha_w + \alpha_s)r} \tag{1}$$

where V_{rms} (Volts) is the root mean square of the amplitude of the voltage recorded by the instrument, $\overline{V_{rms}^2}$ is the quadratic average of V_{rms} over a large number of sonar pings, r (m) is the range from the transducer, ψ is a near field correction (Downing et al., 1995), k_t (V.m$^{3/2}$) is a calibration constant specific to the instrument (Betteridge et al., 2008), s_v (m^2.m^{-3}) is the volume backscattering coefficient (Medwin & Clay, 1998) and α_w and α_s (m^{-1}) are the sound attenuation due to water and suspended particles, respectively. In the following, we will ignore ψ as all the measurements will be made in the far field of the transducers ($\psi = 1$).
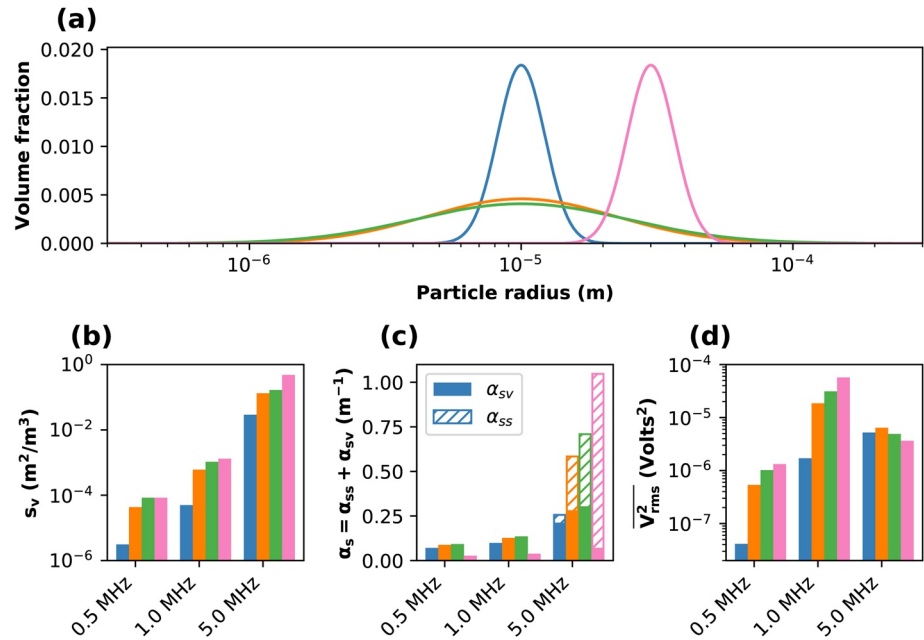
Figure 1. Examples of acoustic model results for spherical particles, with a suspended sediment concentration of 4 g/l, for three frequencies. (a) Synthetic Particle Size Distributions (PSDs) used for the computation. (b) Backscatter (s_v) for the corresponding PSD, the color of the bar corresponds to the PSD represented with the same color. (c) Sediment attenuation (α_s): contributions of scatter (α_{ss}) and viscous (α_{sv}) effects. (d) Resulting synthetic signal $\overline{V_{rms}^2}$ at $r = 1$ m.

Both attenuation and backscattering depend on the suspended sediment concentration and the particles properties. The volume backscattering coefficient for a suspension of spherical particles of radius a, density ρ_s and mass concentration M can be expressed as:

$$s_v = \frac{3}{16\pi} K^2 M \tag{2}$$

where $K = f_\infty / \sqrt{a \rho_s}$ describes the backscattering properties of the particles and f_∞ is the backscattering form factor. This form factor depends on the frequency of the emitted pulse and the particle properties. For natural quartz sand particles, this form factor depends solely on ka where k is the wave number of the emitted sound (see Thorne & Hanes, 2002, among others). Note that in the deep Rayleigh regime where $ka \ll 1$, f_∞ is proportional to $(ka)^2$.

Sediment attenuation α_s is due to both viscous and scattering effects and can be expressed for a suspension of spherical particles of radius a, density ρ_s and mass concentration M as:

$$\alpha_s = \alpha_{sv} + \alpha_{ss} = \frac{3M}{4a\rho_s}(\chi_{sv} + \chi_{ss}) \tag{3}$$

where χ_{sv} and χ_{ss} are the normalized viscous and scattering total cross-sections, respectively.

Conventional models are used in this work, considering a particle size distribution rather than a single size, spherical and oblate particle shapes for viscous attenuation, and a generic model for backscatter or a mica particles-specific one that also should better represent plate-like particles. Models and equations are provided in Appendix A.

Results of s_v, α_{sv} and α_{ss}, computed using spherical models for four synthetic PSDs are presented in Figure 1. The resulting signal $\overline{V_{rms}^2}$ at $r = 1$ m highly depends on the PSD and the frequency, as a result of backscatter and attenuation variations. Backscatter s_v increases drastically with sediment size for all frequencies (compare blue and pink bars, Figure 1b). Thus, even slight differences in sediment distribution widths can lead to significant differences in backscatter and recorded signal (see orange and green

PSDs, Figures 1b and 1d). Attenuation combines viscosity and scattering effects so that the size dependency is more complex (see Figure 1c). This Figure 1 is meant for clarifying the analysis of our results all along this article.

2.2. Inversion Methods

2.2.1. Overview

A number of inversion methods inverting the SSC from measured backscatter (s_v) have been developed in the last three decades for coastal applications (Hay & Sheng, 1992; Hurther et al., 2011 Thorne et al., 2011; Thosteson & Hanes, 1998; Wilson & Hay, 2015, among others). These methods were mainly designed for inverting sand suspension SSC profiles. When the suspension can be assumed homogeneous, as is the case of our experiments, the inversion process simplifies substantially, as the sonar equation (Equation 1) becomes explicit.

Two pieces of information, α_s and s_v, can be extracted for each acoustic frequency. For example, a single-frequency ADCP can be used in rivers to measure the fine sediment and sand acoustic responses separately (Hanes, 2012; Topping & Wright, 2016; Topping et al., 2007; Wright et al., 2010). When only fine sediments are present, both the SSC and particle size can be retrieved from single-frequency α_s and s_v measurements.

When both backscatter (s_v) and attenuation (α_s) are measured at various frequencies, one can use all this information to retrieve SSC and some other sediment characteristics. To limit the number of parameters to be estimated and keep the inversion methods as robust as possible, the shape of the particle size distribution can be fixed. Generally, we assume a lognormal volume PSD:

$$n_v(a) = \frac{1}{a\sigma\sqrt{2\pi}}e^{-((\log_e(a)-\mu)^2/2\sigma^2)} \tag{4}$$

where $n_v(a)$ is the volume particle radius distribution, $\mu = \log_e(a_0)$ where a_0 is the median radius of the volume PSD, and σ is PSD width. In this case, the sediment size characteristics to be estimated are a_0 and σ. These PSD parameters are gathered in a variable noted $\boldsymbol{\theta}$, along with other particle parameters such as the spheroid aspect ratio (h) for oblate particles, when needed. This aspect ratio h is defined as the ratio between the semiminor and semimajor axis of an oblate particle.

The choice of a lognormal volume particle size distribution can be discussed as the PSD encountered in some flows can be significantly different from lognormal, but like most of the existing inversion methods, we did this standard assumption in most of our inversion methods.

However, in some cases, we assumed a bimodal distribution for sediments. The PSD is then described as follows:

$$\begin{aligned} n_v(a) \quad = \quad & w_1 \frac{1}{a\sigma_1\sqrt{2\pi}}e^{-((\log_e(a)-\mu_1)^2/2\sigma_1^2)} \\ & + (1-w_1)\frac{1}{a\sigma_2\sqrt{2\pi}}e^{-((\log_e(a)-\mu_2)^2/2\sigma_2^2)} \end{aligned} \tag{5}$$

$$\mu_1 = \log_e(a_1) \qquad \mu_2 = \log_e(a_2) \qquad 0 \le w_1 \le 1$$

where a_1 and a_2 are the mean radii of the two modes, with respective PSD widths σ_1 and σ_2 and w_1 is the relative weight of the first mode.

In this study, four inversion methods are tested to retrieve the SSC from the acoustic signal, in the simplest case where the suspension is homogeneous along the acoustic beams. The four methods tested are representative of a broader range of existing inversion methods based on backscatter (Method 1), attenuation

Table 1
Detail of the Various Implementations of the Four Inversion Methods Tested

Inversion method	Case	PSD	Viscous att. model (α_{sv})	Scat. models (s_v & α_{ss})	Obj. func.	Fixed parameters	Estimated parameters	Inverse SSC outputs
Method 1 multi-freq. based on s_v	M1.1	lognorm.	-	Generic	Φ	$\sigma = 0.88$	M, a_0	Largely underestimated SSC, Figure 8a
	M1.2	lognorm.	-	Generic	Φ	-	M, a_0, σ	Largely underestimated and scattered SSC, Figure 8a
	M1.3	lognorm.	-	Mica-specific	Φ	$\sigma = 0.88$	M, a_0	Largely underestimated SSC, Figure 8a
Method 2 multi-freq. based on α_s	M2.1	lognorm.	Spheres	Generic	Φ or Γ	$\sigma = 0.88$	M, a_0	Underestimated SSC (Γ), largely scattered SSC (Φ)
	M2.2	lognorm.	Spheres	Generic	Φ or Γ	-	M, a_0, σ	Largely scattered SSC
	M2.3	lognorm.	Oblate spheroids	Mica-specific	Φ or Γ	$\sigma = 0.88$ $h = 1/40$	M, a_0	Relatively accurate SSC when using Γ obj. func., Figure 9a; good a SSC output trend but low values overestimated (Φ), Figure 9b
	M2.4	lognorm.	Oblate spheroids	Mica-specific	Φ or Γ	$h = 1/40$	M, a_0, σ	A good SSC output trend (Γ), overestimated SSC (Φ)
	M2.5	lognorm.	Oblate spheroids	Mica-specific	Φ or Γ	$\sigma = 0.88$	M, a_0, h	Largely scattered SSC
Method 3 single-freq. based on s_v and α_s	M3	lognorm.	Spheres	Generic	-	$\sigma = 0.88$	M, a_0	Fairly accurate SSC, Figure 10a
Method 4 multi-freq. based on s_v and α_s	M4.1	lognorm.	Spheres	Generic	E	-	M, a_0, σ	Underestimated SSC, Figure 12a
	M4.2	bimodal	Spheres	Generic	E	-	$M, a_1, a_2, \sigma_1,$ σ_2, w_1	Underestimated SSC, Figure 12b
	M4.3	lognorm.	Oblate spheroids	Mica-specific	E	$1/40 \leq h \leq 1$	M, a_0, σ	Fairly accurate SSC, Figure 12c
	M4.4	lognorm.	Oblate spheroids	Mica-specific	E	-	M, a_0, σ, h_{min}	Fairly accurate SSC, Figure 12d

Note. It includes the PSD model used, either lognormal or bimodal; the viscous attenuation model used, either Urick (1948) spherical model or Richards et al. (2003) oblate spheroid model; the scattering model used for s_v & α_{ss}, either the generic model or the mica-specific model of Moate and Thorne (2012), see Appendix A; the objective function used, if any; the parameters fixed prior to the inversion, if any; the inverted parameters; and a comment on SSC inversion outputs eventually indicating the corresponding figure.

PSD, Particle Size Distribution; SSC, suspended sediment concentration.

(Method 2), or both (Method 3). Method 4 is an original development including more advanced options/representations of the particles. The various implementations tested are summarized in Table 1.

Method 1 is taken from Thorne and Hurther (2014). It is representative of the many inversion methods developed in acoustical oceanography for measuring sand suspensions. The inversion algorithm uses backscatter information (s_v) at various frequencies. In implementations M1.1 and M1.2 (see Table 1), in addition to M (the SSC), $\boldsymbol{\theta} = (a_0)$ and $\boldsymbol{\theta} = (a_0, \sigma)$ are estimated, respectively. In implementation M1.3, the alternative mica-specific model is tested and $\boldsymbol{\theta} = (a_0)$ is estimated.

Method 2 was proposed by Moore et al. (2013). It was designed for measuring river fine sediment suspensions with uncalibrated ADCPs. The inversion algorithm uses attenuation information (α_s) at various frequencies. In implementations M2.1 and M2.2, $\boldsymbol{\theta} = (a_0)$ and $\boldsymbol{\theta} = (a_0, \sigma)$ are estimated, respectively, using

a viscous attenuation model for spheres and the generic model of Moate and Thorne (2012) for scattering. In implementations M2.3, M2.4, and M2.5, $\boldsymbol{\theta} = (a_0)$, $\boldsymbol{\theta} = (a_0, \sigma)$, and $\boldsymbol{\theta} = (a_0, h)$ are estimated, respectively, using a viscous attenuation model for oblate spheroids and the mica-specific model of Moate and Thorne (2012) for scattering.

Method 3 uses the ratio of attenuation to backscatter at only one frequency; $\boldsymbol{\theta} = (a_0)$ is estimated. Such a method was also applied by Guerrero and Di Federico (2018) and Aleixo et al. (2020).

Method 4 uses both backscatter and attenuation information at various frequencies. Viscous attenuation models for spheres (M4.1 and M4.2) and oblate spheroids (M4.3 and M4.4) are tested, and accordingly, the generic model (M4.1 and M4.2) or mica-specific model (M4.3 and M4.4) for scattering. In implementations M4.1, M4.3, and M4.4, $\boldsymbol{\theta} = (a_0, \sigma)$, $\boldsymbol{\theta} = (a_0, \sigma)$, and $\boldsymbol{\theta} = (a_0, \sigma, h_{\min})$ are estimated, respectively. In implementation M4.2, we assumed a bimodal particle size distribution and $\boldsymbol{\theta} = (a_1, a_2, \sigma_1, \sigma_2, w_1)$ is estimated.

The next sections describe the four inversion methods in more detail as well as their various implementations.

2.2.2. Method 1: Multifrequency Backscatter Inversion

We used the algorithm of Thorne and Hurther (2014), that minimizes the objective function Φ:

$$
\begin{aligned}
\Phi(\boldsymbol{\theta}) &= \frac{\delta_M(\boldsymbol{\theta})}{M_0(\boldsymbol{\theta})} \\
M_0(\boldsymbol{\theta}) &= \frac{1}{N} \sum_{j=1}^{N} M_{0,j}(\boldsymbol{\theta}) \\
\delta_M^2(\boldsymbol{\theta}) &= \frac{1}{N} \sum_{j=1}^{N} M_{0,j}^2(\boldsymbol{\theta}) - [M_0(\boldsymbol{\theta})]^2
\end{aligned}
\tag{6}
$$

where N is the number of frequencies explored, $M_{0,j}(\boldsymbol{\theta})$ is the model-computed SSC that matches s_v measurement for the jth frequency, using the particle parameters set $\boldsymbol{\theta}$ in the backscatter model. Here, $\boldsymbol{\theta}(a_0, \sigma)$ are the parameters of the lognormal PSD.

In implementation M1.1 (see Table 1), σ is fixed prior to the inversion: only a_0 is inverted along with SSC, similarly to what Thorne and Hurther (2014) did. In implementation M2.2, we also tried to invert σ along with a_0 and SSC. In implementation M2.3, s_v is computed using the mica-specific model proposed by Moate and Thorne (2012) instead of the generic model. This model was tested as it applies to particles having a flatter shape that may be more representative of the particles used in this study. In any configuration, the parameters set $\boldsymbol{\theta}_{\min}$ where Φ is found to be minimal is used to retrieve both PSD and concentration (SSC = $M_0(\boldsymbol{\theta}_{\min})$).

2.2.3. Method 2: Multifrequency Attenuation Inversion

Moore et al. (2013) attenuation-based method minimizes the objective function Γ:

$$
\Gamma(\boldsymbol{\theta}) = \sum_{i=1}^{N} \sum_{j>i}^{N} |M_{0,i}(\boldsymbol{\theta}) - M_{0,j}(\boldsymbol{\theta})|
\tag{7}
$$

where $M_{0,i}(\boldsymbol{\theta})$ and $M_{0,j}(\boldsymbol{\theta})$ are the model-computed SSCs that match the $\alpha_{s,i}$ and $\alpha_{s,j}$ measurements for the ith and j^{th} frequencies, respectively—using the particle parameter set $\boldsymbol{\theta}$ in the attenuation model. The parameter set $\boldsymbol{\theta}_{\min}$ where Γ is found to be minimal is used to retrieve the sediment characteristics and concentration (SSC = $\frac{1}{N} \sum_{i=1}^{N} M_{0,i}(\boldsymbol{\theta}_{\min})$). In this study, we also tried to use the alternative objective function Φ (Equation 6) instead of Γ. The Φ and Γ objective functions describe 2-norm (Euclidean distance) and 1-norm solutions, respectively. Whereas the 1-norm is less sensitive to outliers, the 2-norm statistically offers the most likely solution (least squares solution) if the data errors are normally distributed.

Following the work of Moore et al. (2013), we tested both the spherical particle model of Urick (1948) (see Appendix A, Equation A12) and the oblate spheroid model of Richards et al. (2003) (see Appendix A) for modeling sediment viscous attenuation. Note that the oblate spheroid model requires an extra parameter h known as the particle aspect ratio. When using the spherical model (implementations M2.1 and M2.2 in Table 1), we used the generic model of Moate and Thorne (2012) for the scattering attenuation in α_s computation (Equation A10). When using the oblate spheroid model (implementations M2.3, M2.4, and M2.5), the mica-specific model was preferred (Equation A11).

In Moore et al. (2013), only a_0 was inverted along with SSC. In the present study, we also tried to invert more parameters (σ or h) as detailed in Table 1.

2.2.4. Method 3: Single-Frequency Backscatter and Attenuation Inversion

In this method (implementation M3 in Table 1), both information on α_s and s_v are used to retrieve SSC and particle size at one frequency. The PSD width (σ) is fixed prior to the inversion. The theoretical ratio of attenuation to backscatter is computed for various a_0:

$$\frac{\alpha_s}{s_v} = \frac{4\pi \int_0^\infty a^2 \left[\chi_{sv}(a) + \chi_{ss}(a) \right] n(a) da}{\int_0^\infty a^2 f_\infty^2(a) n(a) da} \tag{8}$$

Note that this ratio does not depend on SSC. In Equation 8, χ_{sv} is computed from Urick (1948) spherical model (Equation A12) and f_∞ and χ_{ss} are computed from Moate and Thorne (2012) generic model (Equations A4 and A10, respectively). The value of a_0 that leads to the empirically measured α_s/s_v ratio is then used to retrieve SSC from attenuation (cf. Equation A9):

$$M = \alpha_s \frac{4\rho_s \int_0^\infty a^3 n(a) da}{3\int_0^\infty a^2 \left[\chi_{sv}(a) + \chi_{ss}(a) \right] n(a) da} \tag{9}$$

2.2.5. Method 4: Multifrequency Backscatter and Attenuation Inversion

In this method, a data set of modeled α_s and s_v values is generated at each frequency for various SSCs and various sets of particle parameters. In practice, the particle parameter set $\boldsymbol{\theta}$ includes PSD parameters, plus the aspect ratio h_{min} (see below) when using the oblate spheroid model of Richards et al. (2003) for computing viscous attenuation. Inverse SSC and particle parameters ($\boldsymbol{\theta}$) are sought by minimizing the following objective function:

$$\mathrm{E}(\boldsymbol{\theta}) = \sum_{j=1}^{N} \left(A_j^2 \left| \frac{\hat{\alpha}_{s,j} - \alpha_{s,j}}{\alpha_{s,j}} \right|^2 + A_j \left| \frac{\hat{s}_{v,j} - s_{v,j}}{s_{v,j}} \right|^2 \right) \tag{10}$$

where $\hat{\alpha}_{s,j}$, $\alpha_{s,j}$, $\hat{s}_{v,j}$ and $s_{v,j}$ are the jth frequency modeled and measured sediment attenuation, and the modeled and measured backscatter, respectively. The weighting terms A_j are defined as:

$$A_j = \begin{cases} (f_j/f_0)^3 & \text{if } \alpha_{s,j} > 0.1\,\text{m}^{-1} \\ 0 & \text{if } \alpha_{s,j} \leq 0.1\,\text{m}^{-1} \end{cases} \tag{11}$$

where f_j is the jth frequency in MHz and $f_0 = 1.0$ MHz. Weighting terms A_j were introduced to account for the fact that higher frequencies provide more reliable information than lower ones, because α_s and s_v are greater. In the critical case of a very low attenuation ($\alpha_s < 0.1\,\text{m}^{-1}$, as observed at low frequency and low concentration), the acoustic information is considered too imprecise to be taken into account, and then is removed from the inversion process. More importance is also given to sound attenuation (α_s) than to backscatter (s_v) by weighting α_s information with A_j^2, because α_s is more sensitive to SSC and because an error in α_s measurement will induce an error in s_v estimate. The choice of the weights was arbitrary: they were chosen because of their capacity to improve inversion outputs. Obviously, further research on model and measurement uncertainties would help improve these coefficients.
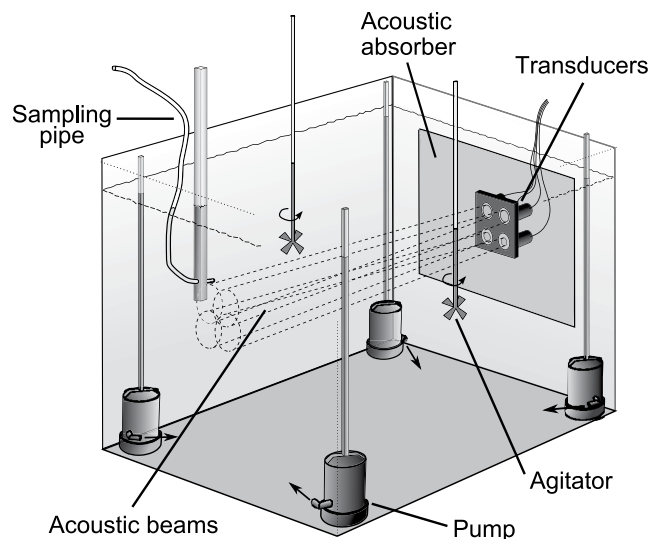
Figure 2. Experimental tank ($1 \times 1 \times 1$ m) used in this study. A second tile of acoustic absorber was fixed on the wall facing the transducers (not shown here).

This method was tested in four different implementations (cf. Table 1). In case M4.1, a lognormal PSD was used to model the particle size, the viscous attenuation was computed from Urick (1948) spherical model (Equation A12) and the scattering processes with the generic model of Moate and Thorne (2012) (see Equations A4 and A10). In case M4.2, the lognormal PSD was replaced by a bimodal PSD. In cases M4.3 and M4.4, viscous attenuation was computed using Richards et al. (2003) oblate spheroid model and scattering processes were computed using the mica-specific model of Moate and Thorne (2012) (see Equations A5 and A11). As smaller particles tend to be flatter, we set the particle aspect ratio h to a constant value $h_{\min}$ lower than one, that corresponds to flat oblate spheroids, when the particle radius was small ($a \leq 1\,\mu$m); and we set $h = 1$ (spheres) for $a \geq 30\,\mu$m. Between these two bounds, we made the h increase linearly with a. In case M4.3, the value of $h_{\min}$ for the finer particles ($a \leq 1\,\mu$m) was fixed prior to the inversion. In case M4.4, the value of $h_{\min}$ was also inverted.

2.3. Experimental Facility

2.3.1. Description of the Experimental Facility

To create a homogeneous suspension with fine river sediments, we used a 1 m³ tank (Figure 2) filled with fresh water 2 days before the start of the experiment, in order to let the water degas. Four submerged pumps and two propeller agitators were fixed on rods into the tank to generate turbulence and keep the sediments in suspension. When needed, the orientation of the submerged pumps could be varied remotely to re-suspend some sediments trapped at the bottom and gently raise the concentration without air injection. Water samples were taken within the tank using a 5 mm pipe connected to a peristaltic pump. Extensive sampling in the tank showed that the PSD and the concentration were fairly homogeneous in space, with a standard deviation of 1.5% of the mean in SSC between the 12 sampling point locations tested. PSD remained fairly constant in time while SSC was decreasing very slowly (~0.2 g/l/hr). Good suspension homogeneity was therefore achieved during each acoustic measurement (~4 min). Water temperature was continuously recorded and remained constant around 35 ± 1°C during all the experiment. This high temperature was due to submerged pumps heating. We estimated that the uncertainty of water temperature measurement is 0.1°, which leads to approximately 0.5% uncertainty on the water attenuation.

A multifrequency ABS Aquascat 1000R was deployed horizontally in the tank using four transducers at the same time but spanning 6 frequencies (0.3, 0.5, 1.0, 2.5, 4.0, and 5.0 MHz) using the transducers alternatively. Unfortunately, strong ambient noise as well as strong backward reflections prevented us from using the 0.3 MHz data. In retrospect, this strong ambient noise might come from too small acoustic bin size (5 mm). A tile of ultrasonic absorber (Aptflex F28, Precision Acoustics) was put behind and in front of the transducers in order to reduce unwanted backward reflections at 0.5 MHz and decrease the time of sound dissipation between two sonar pings. Ping frequency was set to 8 Hz. In the following, one acoustic measurement refers to the average profile computed in quadratic mean over 2,000 or more successive pings. The instrument had been previously calibrated by the manufacturer on a suspension of glass beads following the Betteridge et al. (2008) procedure.

Submerged pumps were producing a relatively small and constant amount of air micro-bubbles. The backscatter signal of bubbles was recorded in clear water prior to the injection of sediments, after letting the pumps run for 1 day. We measured a sensitivity to air micro-bubbles that increases with frequency up to 1.0 MHz and decreases thereafter. Overall, air micro-bubble acoustic backscatter was found to be relatively weak, with a Signal to Noise Ratio (SNR) below 10 most of the time. The SNR was computed as the ratio of
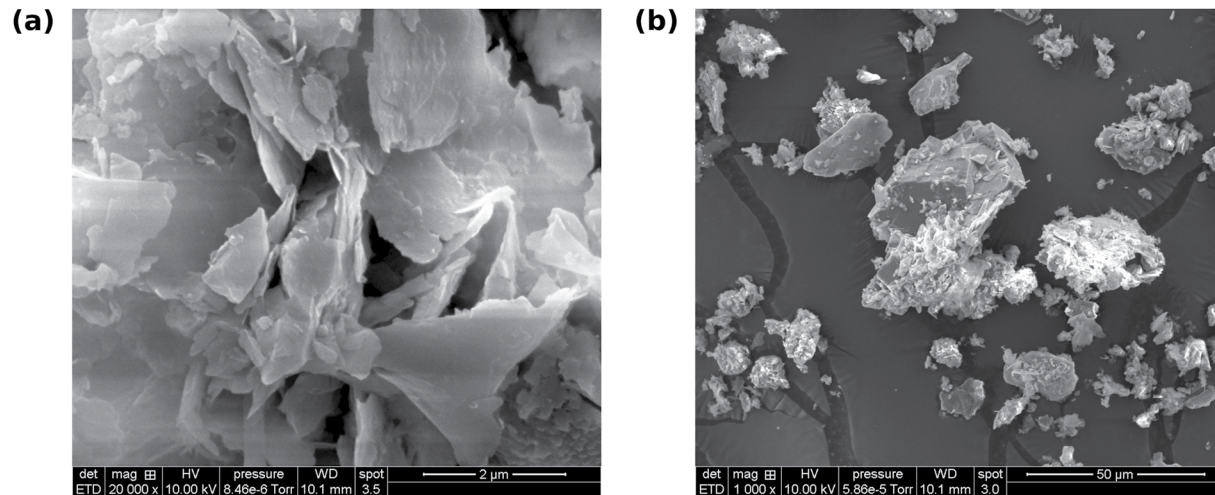
Figure 3. Scanning electron microscope images of suspended sediment particles collected from the tank: (a) small clay platelets, (b) bigger angular silt particles.

the backscatter signal to the ambient noise signal recorded without pulse emission. Sound attenuation due to air micro-bubbles was found to be negligible compared to sediment attenuation.

Wet sediments were injected gradually from the free surface in order to increase the concentration progressively. Freshwater was also added at the end of the experiment to dilute the concentration. Acoustic measurements related to one concentration were handled one night after each injection/dilution to let the temperature and micro-bubble concentration stabilize. At the very end of the experiment, we did additional acoustic measurements as the pumps were turned off, to study lower concentrations and smaller suspended particles. These data were excluded from specific analysis requiring constant PSD data.

2.3.2. Sediment Particles Characterization

We used natural river sediments collected from a deposition area upstream of the lock of Belley in the Rhône River, France (Lat., Long. = 45.77, 5.76). The sediments were mainly clay, with a small fraction of silt (median diameter $D_{50} \approx 14.6\,\mu\text{m}$, with 10% of the particles in mass being larger than $D_{90} \approx 40\,\mu\text{m}$). For the frequencies used in this study, these sediments lead a product ka ranging between 2.10^{-3} and 2. Sediments were sieved at 500 μm prior to the experiment to remove coarse organic matter. A Cilas 1190 laser grain-sizer was used to measure the PSD because of the capacity of laser diffraction technology to measure small particles (down to ~1 μm). Ultrasounds were applied to the samples before the measurements in order to break potential flocs and have access to the primary particle size. Acoustic models need the number density $n(a_i)$ of the PSD instead of the volume density $n_v(a_i)$ provided by a laser grain-sizer. To convert the volume PSD to number PSD, we assumed a statistically spherical shape of the particles and used the relation:

$$n(a_i) = \frac{1}{\Delta a_i} \frac{n_v(a_i)/a_i^3}{\sum_i n_v(a_i)/a_i^3}$$

(12)

where a_i (m) is the radius of the ith size class of the laser grain-sizer and $\Delta a_i = a_{i+1} - a_i$.

As expected for natural fine sediments, the particles were far from being spherical however. A large diversity in shape was observed when looking at particles collected from the tank suspension with a scanning electron microscope (SEM, Figure 3). Small clay particles look like fine and flat platelets (Figure 3a) while bigger particles (> 30 μm) are more similar to angular and irregular polyhedrons (Figure 3b). The definition and the measurement of one single parameter for describing the size of highly irregular particles is challenging. Even if this problem was circumvented with the assumption of statistically spherical, randomly oriented particles, large uncertainties could come out in the micron and sub-micron ranges when measuring PSD by laser diffraction (Eshel et al., 2004). Comparing Cilas 1190 measurements with a Malvern

Mastersizer 2000 on some samples, we found an almost equal D_{50} but somewhat different PSD shape (not shown here). This illustrates the difficulties for precisely measuring the PSD in the case of small particles.

Assuming a spheroidal shape instead of a spherical shape for the particles could help to better take the specific shape of fine particles into account. Indeed, as shown by Schaafsma and Hay (1997), in a spherical approximation, the particle equivalent radius can relate to different quantities depending on the physical process that is considered. When converting mass or volume concentration to number of particles, particle radius relates the radius of a sphere having the same volume as the particle. When considering scattering processes as backscattering and scattering attenuation, particle radius relates to the radius of a sphere having the same geometrical cross-section. Finally, when looking at viscous attenuation, particle radius relates to the radius of a sphere having the same outer surface. These different definitions illustrate the complexity of determining a single "particle equivalent radius" for highly nonspherical particles like fine sediments.

Suspended sediment mass concentrations were estimated by filtering the water samples using 0.45 µm glass fiber filters. The uncertainty of this method for the concentrations observed in the tank is estimated to be ±5%. This value was estimated considering the works of Dramais (2020); Orwin and Smart (2004); Gordon et al. (2000).

For each acoustic measurement, four water samples of 100 ml on average were taken in the tank within the acoustic beams: two samples at ~30 cm from the transducers and two samples at ~60 cm. For each location, one sample was used to estimate the SSC, and the other was used to estimate the PSD. We did not observe any significant difference in SSC nor PSD between the two sampling locations so we took the average as the final measured value.

Sediment density in general, and clay density in particular, may deviate from the typical value of $2{,}650\ \mathrm{kg\,m^{-3}}$ used in many studies. For instance, in a study of numerous soil samples, Schjønning et al. (2017) found a mean clay density of $2{,}886\ \mathrm{kg\,m^{-3}}$. Unfortunately, we were not able to measure ρ_s in the present study. Nevertheless, sediment density plays a role at various stages in acoustic modeling: to compute the number of particles per unit volume from SSC and PSD, to model viscous attenuation (related to the inertia of the particles) and to model scattering processes. Note that the empirical formulas for scattering used in this work (Moate & Thorne, 2012) already include density variability so that sensitivity to this parameter could not be tested. In the following, we assume the sediment density to be equal to $2{,}650\ \mathrm{kg\,m^{-3}}$.

2.3.3. Attenuation and Backscatter Measurements

For each acoustic measurement averaged over many sonar pings as explained in Section 2.3.1, the sediment attenuation coefficient (α_s) was estimated using the Fluid Corrected Backscatter (FCB):

$$
\begin{aligned}
\mathrm{FCB} &= \frac{1}{2}\log_e\left(\overline{V_{rms}^2}\, r^2 \mathrm{e}^{4r\alpha_w}\right)\\
&= \frac{1}{2}\log_e\left(\frac{16\pi k_t^2}{3}s_v(r)\right) - 2r\alpha_s(r)
\end{aligned}
\tag{13}
$$

For a homogeneous suspension, $k_t^2 s_v$ is constant along the acoustic path and α_s is given by the FCB slope:

$$
\alpha_s = -\frac{1}{2}\frac{\mathrm{dFCB}}{\mathrm{dr}}
\tag{14}
$$

Figure 4a shows an example of FCB profiles measured during the experiment, with the intercepts set to 0 for $r = 0$ in order to make it easier to compare the slopes at different frequencies. The FCB varies fairly linearly with the range r, which confirms the suspension homogeneity.

The volume backscattering coefficient (s_v) was estimated with Equation 1 using the empirical value of α_s obtained from Equation 14. Figure 4b shows an example of s_v profiles measured during the experiment. As expected for a homogeneous suspension, s_v is fairly constant with range. In the following, s_v will be averaged along the acoustic profile.

We were not able to measure s_v for frequencies lower than 1.0 MHz due to the very weak target strength of fine sediments at low frequency (cf. Figure 1b) that results in a recorded signal close to the noise level. We
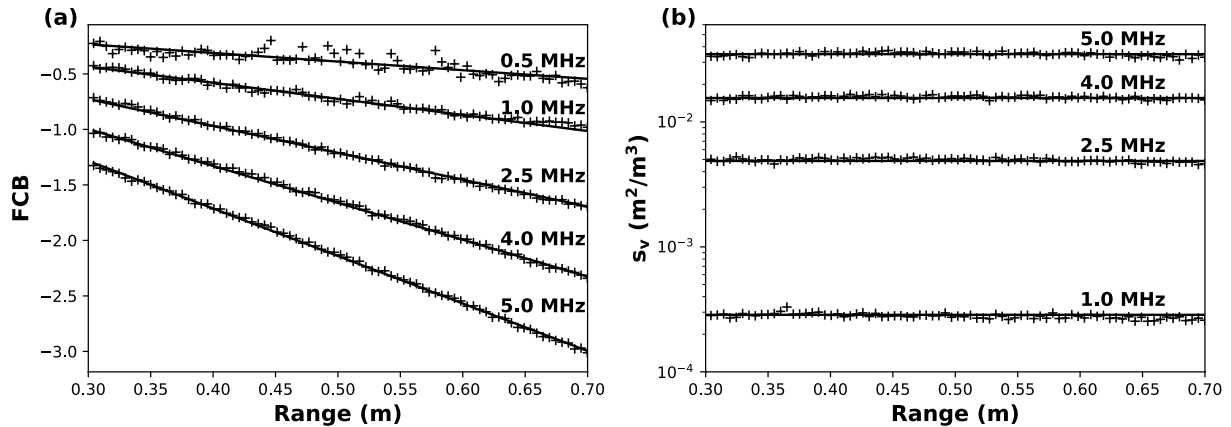
Figure 4. Example of profiles (crosses) with linear fit recorded in the tank for $M \approx 9.5$ g/l: (a) fluid corrected backscatter (FCB); (b) volume backscattering coefficient (s_v). The intercepts of the FCB profiles were set to 0 for $r = 0$ to make the slopes comparison easier.

observed noise influence for SNR lower than 10, a threshold consistent with other studies using sonar (e.g., Gostiaux & van Haren, 2010). Note that noise issues related to fine sediment low backscatter signal are also encountered in field deployment (e.g., Haught et al., 2017).

Because air micro-bubbles had negligible influence on attenuation, we estimated α_s provided that the recorded backscatter signal was sufficiently strong compared to the ambient noise signal. Therefore, α_s was estimated for all the acoustic profiles or part of the acoustic profiles where $\mathrm{SNR}_{\mathrm{amb}} = \overline{V_{rms}^2}/\overline{V_{amb}^2} > 10$, where $\overline{V_{amb}^2}$ is the ambient noise recorded in the tank without sonar ping emission. Conversely, air micro-bubbles signal could potentially affect s_v measurements. To overcome this problem, s_v was estimated only for range cells where $\mathrm{SNR}_{\mathrm{bub}} = \overline{V_{rms}^2}/\overline{V_{bub}^2} > 10$, where $\overline{V_{bub}^2}$ is the bubble backscatter signal recorded in the tank filled with clear water prior to sediment injection.

2.3.4. Attenuation and Backscatter Versus SSC

Figure 5a shows the relations between SSC and α_s in the tank at various frequencies. As predicted by the theory when multiple scattering can be neglected and as observed in numerous other studies (e.g., Hay, 1991; Hunter et al., 2012; Moore et al., 2012; Sung et al., 2008; Rice et al., 2014; Urick, 1948, among others), there is a good linear relation between sound attenuation and sediment concentration (cf. Table 2).
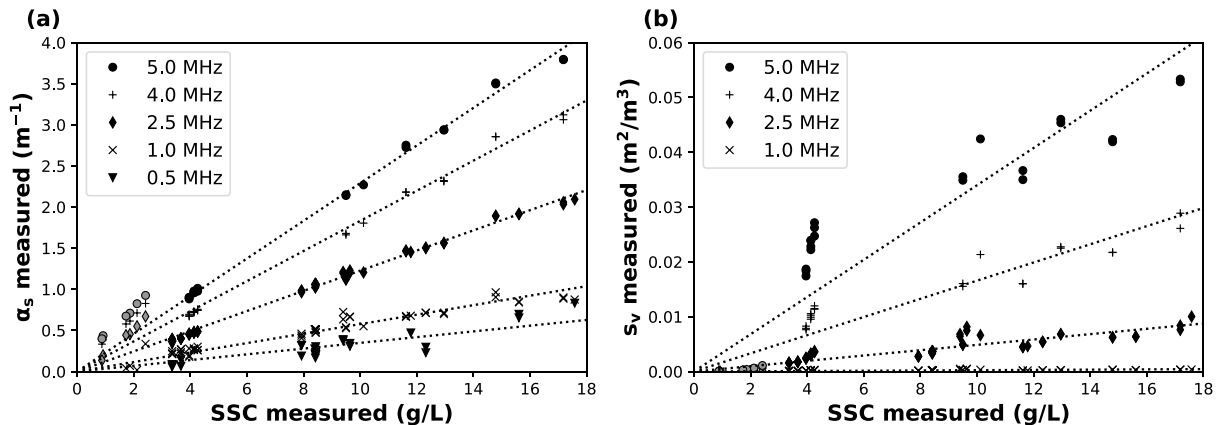
Figure 5. Measured suspended sediment concentration versus (a) measured sediment attenuation (α_s) and (b) range-averaged measured volume backscattering coefficient (s_v). Dashed lines are regression lines forced to the origin computed for constant Particle Size Distribution (PSD) data. Gray points indicate that the pumps were turned off in the tank and correspond to different PSD.

Table 2
Linear Relations (R^2 and Slope With 95% Confidence Interval) of Attenuation (α_s) Versus SSC and Backscatter (s_v) Versus SSC, Computed for SSC > 3 g/l in the Experimental Tank

Frequency	Attenuation		Backscatter	
	R^2	Slope (l.g^{-1}.m^{-1})	R^2	Slope (l.g^{-1}.m^{-1})
0.5 MHz	0.63	0.035 ± 0.001	-	-
1.0 MHz	0.95	0.058 ± 0.002	0.60	$0.02 \pm 0.003 \times 10^{-3}$
2.5 MHz	0.99	0.123 ± 0.003	0.81	$0.49 \pm 0.032 \times 10^{-3}$
4.0 MHz	0.99	0.183 ± 0.003	0.91	$1.66 \pm 0.11 \times 10^{-3}$
5.0 MHz	0.99	0.229 ± 0.005	0.87	$3.40 \pm 0.26 \times 10^{-3}$

Note. SSC, suspended sediment concentration.

Linear relations between s_v and SSC are not as good however (Figure 5b, Table 2). This is probably due to the very small target strength of fine sediments. Note that as the pumps were turned off at the very end of the experiment—which corresponds to SSC < 3 g/l (gray points) in Figure 5—mean particle size decreased and it modified the slope of the relations of α_s and s_v to SSC. Therefore, dashed regression lines in Figure 5 as well as the values presented in Table 2 have been computed excluding these variable PSD data (see Figure 7). Note also that the slopes of the relation of s_v to SSC for the different frequencies should be linearly related in the Rayleigh regime. This is not what we observed, most probably because of the uncertainty in s_v determination for such fine sediment and because we did not considered a single grain size but poorly sorted sediment with a wide PSD.

The attenuation versus SSC slopes presented in Table 2 are consistent with values obtained in other similar river sediment studies (e.g., Moore et al., 2012, Table 4). Note that sediment attenuation not only presents a better linear relation with SSC (higher R^2), but is also ~100 times more sensitive to fine SSC than s_v is. For these reasons, sound attenuation is a better proxy than backscatter for calibrating an ABS or an ADCP in relation to fine SSC. This type of calibration is more effective when using high frequencies, as the sensitivity to SSC increases while the uncertainty in the determination of FCB slope decreases. Such calibration is however very sensitive to any change in the particle characteristics, and particularly in the PSD as confirmed by the gray points in Figure 5a that deviates from the linear relation.

3. Acoustic Model Performances

3.1. Evaluation of Acoustic Model Outputs

Acoustic model outputs were compared to the measurements (cf. Figure 6, black symbols). The theoretical α_s and s_v from the equations presented in Appendix A were computed from the SSC and PSD data measured from water samples. Sediment viscous attenuation was computed from Urick (1948) spherical model, and scattering attenuation and backscatter with the generic model of Moate and Thorne (2012) in a first step (option S, in Figures 6a and 6b). Scattering attenuation accounts for ~15% of total sediment attenuation (α_s) at 5.0 MHz, and less than 2% at 2.5 MHz or below. Acoustic modeling was performed using the SSC and PSD associated to each acoustic measurement, so that variations of PSD at low concentrations (SSC < 3 g/L, pumps off) are taken into account.

Overall, the attenuation modeled using Urick (1948) spherical model is ~35% lower than the measurements (Figure 6a). This value is consistent with the field study of Haught et al. (2017). Conversely, the modeled backscatter (using the generic model of Moate & Thorne, 2012) is dramatically overestimated by a factor 4 (Figure 6b). Besides the acoustic models themselves, numerous factors can play a role in these discrepancies. Some of these factors are explored in the next sections.
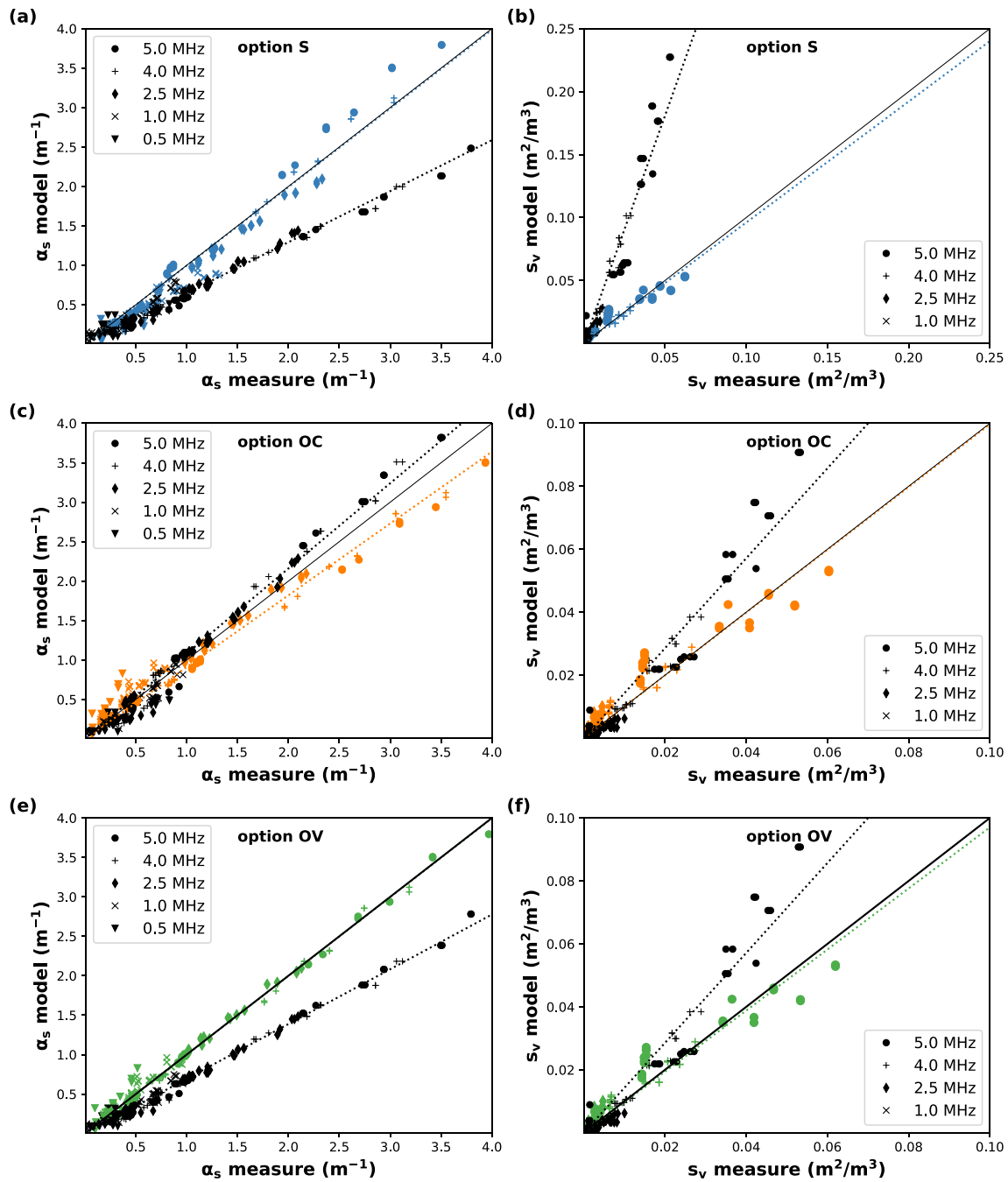
Figure 6. Acoustic model outputs versus measurements for all available sonar frequencies: in black, direct modeling using the Particle Size Distribution (PSD) data measured by laser diffraction; in blue, orange and green, direct modeling using the optimal PSD obtained from the sensitivity test—optimal PSDs are shown in Figure 7 with colors matching the present figure. (a) and (b) Sediment attenuation (α_s) and volume backscattering (s_v) using option S; (c) and (d) option OC; (e) and (f) option OV. Model equations, used parameters, linear regression slopes and goodness of fit R^2 for the three options S, OC, and OV are summarized in Table 3.

3.2. Sensitivity to Particle Shape and Size

Applying previous work of Richards et al. (2003) (see Appendix A), we were able to compute the viscous attenuation for oblate spheroids instead of spheres. The aspect ratio of the spheroids was first set to 1/40 for all particles that corresponds to flat oblate spheroids, as this value was used in other similar studies (Moore et al., 2013; Richards et al., 2003). The scattering attenuation was computed using the mica-specific

model of Moate and Thorne (2012). Mica particles in their work were plate-like and we assume that using this model allows to better take into account the spheroid shape of the particles. The combination of these choices is the option OC in Figure 6 and Table 3. For both computations we also assumed that the output length of the volume probability density function measured with the laser diffraction is the semimajor axis, which is supported by previous work of Erdoğan et al. (2007). Results for modeled attenuation are greatly improved when using the oblate spheroid model instead of the spherical model (compare Figures 6a and 6c). Similarly, even if it is less striking, using the mica-specific model for backscattering also improves s_v results (compare Figures 6b and 6d).

These results are encouraging and we went further assuming that fine and coarse particles have different shapes. Similarly to what has been presented for inversion Method 4, we tested to set the particle aspect ratio h for viscous attenuation to a constant value $h_{min} = 1/40$ when the particle radius was small ($a \leq 1\,\mu m$); and we set $h = 1$ (spheres) for $a \geq 30\,\mu m$. Between these two bounds, we made h increase linearly with a. Results are presented in Figure 6e (option OV). Surprisingly, the agreement between model and measure is not as good as with constant h, the slope of the regression curve between model and measure for α_s decreased from 1.08 to 0.69 (see Table 3). However, a better linear fit can be obtained (R^2 is closer to 1).

To test the sensitivity of the acoustic models to PSD, we searched for a PSD that would improve the agreement between acoustic modeling and measurements. For a measured SSC, we computed α_s and s_v for a set of automatically generated PSDs. PSDs were obtained applying the following simple procedure: (a) the mean measured PSD was fitted with a 2-mode Gaussian mixture model (cf. Masson et al., 2018, for a description of the method); (b) we build new 2-mode Gaussian mixture PSDs with mode centers ranging ±50% from the two initial (fitted from measurement) values and weights from 0 to 1. The PSD width (σ) of the two modes were not changed. A set of ~4,000 PSDs was generated following this method. For the three options (S, OC, and OV), we extracted the "optimal" PSD leading to the best regression slopes, that is closest to 1, between the acoustic model outputs (α_s and s_v) and the measurements. Figure 7 shows the three optimal PSDs obtained from this sensitivity test. Model combinations, regression slopes and R^2 are summarized in Table 3.

In all cases, using the optimal PSD obtained from the sensitivity test instead of the PSDs measured by laser diffraction greatly improved model performances as shown in Figure 6 (compare black and colored symbols). Best optimization results are provided for option OV, assuming an oblate spheroid shape for fine particles with varying aspect ratio h to compute viscous attenuation, and using the mica-specific model for scattering (Figures 6e and 6f). Compared to the mean PSD measured by laser diffraction ($D_{50} = 14.6\mu m$), the optimal PSDs obtained from the sensitivity test are finer ($D_{50} = 7.3\mu m$ for option S; $D_{50} = 4.9\mu m$ for option OC; and $D_{50} = 7.3\mu m$, for option OV, cf. Figure 7). Surprisingly, using option OC did not reduce the gap between measured and optimized PSDs (compare orange dashed line and solid black line in Figure 7) although this model configuration gave the best results with measured PSDs (black symbols in Figures 6c and 6d). Nevertheless, optimized PSDs can be within the margin of uncertainty for each of the three cases and the discrepancies between model outputs and measurements may be due to particles actually finer than what laser diffraction measured, as also observed by Erdoğan et al. (2007).

3.3. Sensitivity to Flocculation

Flocculation in the tank was not directly monitored but was certainly negligible, and otherwise, this could not explain the model errors, at least on backscatter (s_v). Indeed, first, the high turbulence generated by the pumps and the agitators made the presence of large flocs unlikely. Second, for the same mass concentration and same primary particle type, a suspension of flocculated particles leads to larger s_v than a suspension of nonflocculated particles (MacDonald et al., 2013; Rouhnia et al., 2014). As ultrasounds were applied to break potential flocs prior to PSD measurement by laser diffraction, the model outputs in Figure 6 (black symbols) should relate to the primary particles acoustic response. Hence, the modeled s_v (cf. Figures 6b, 6d, and 6f) should be even more overestimated if ever flocs were actually formed in the experimental tank.

Table 3
Summary of the Equations Used to Model Acoustic Response for the Measured PSD or the Optimized PSD

Model option	Attenuation		Slope of regression	
	Viscous α_{sv}	Scattering α_{ss}	Measured PSD	Optimal PSD
S (blue)	Spherical, Equation A12	Generic, Equation A10	0.65, $R^2 = 0.98$	1.00, $R^2 = 0.96$
OC (orange)	Oblate spheroid, Equations A13–A17, $h = 1/40$, constant	Mica-specific, Equation A11	1.08, $R^2 = 0.98$	0.91, $R^2 = 0.97$
OV (green)	Oblate spheroid, Equations A13–A17, $1/40 \le h \le 1$, varies	Mica-specific, Equation A11	0.69, $R^2 = 0.99$	1.00, $R^2 = 0.99$

Model option	Backscatter	Slope of regression	
	s_v	Measured PSD	Optimal PSD
S (blue)	Generic, Equation A4	3.62, $R^2 = 0.95$	1.00, $R^2 = 0.93$
OC (orange)	Mica-specific, Equation A5	1.43, $R^2 = 0.95$	1.03, $R^2 = 0.92$
OV (green)	Mica-specific, Equation A5	1.43, $R^2 = 0.95$	1.00, $R^2 = 0.92$

Note. For each model option, the table summarizes the resulting slopes and goodness of fit R^2. PSD, Particle Size Distribution.
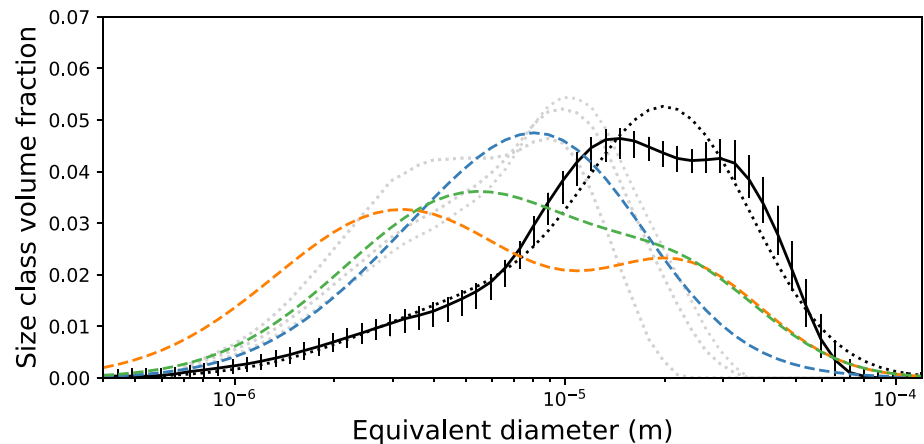
Figure 7. Volume particle size distribution: average of all the laser diffraction measurements (solid black line with error bars including all measurements), excluding the last samples with the pumps off (Particle Size Distribution [PSD] shown as light gray dotted lines); 2-mode Gaussian mixture model fit to the mean PSD (dotted black line); PSD leading to the best agreement between model outputs (α_s and s_v) and the measurements, using the spherical model (option S, dashed blue line) or oblate spheroid model for viscous attenuation, with constant h (option OC, dashed orange line) or varying h (option OV, dashed green line). Model equations and used parameters for these options are summarized in Table 3.

4. Evaluation of Inversion Methods

In this section, we show and discuss some outputs of each of the four inversion methods presented in Section 2.2 (cf. Table 1). The analysis of inversion efficiency is mainly focused on SSC, as this parameter is the most used in river applications, and as SSC is probably the suspension parameter that can be measured with most confidence from water sampling. "True" values of other parameters like particle size are more uncertain, making the comparison with inversion outputs more difficult.

In the following, we sometimes fix the value of the PSD width (σ) to 0.88. This value was obtained by fitting a lognormal distribution to the mean volume PSD measured by laser diffraction. Note that for a lognormal PSD, volume and number distributions share the same σ. In some cases, we also set the particle aspect ratio for fine particles (h or $h_{\min}$) to 1/40 prior to the inversion. We used this value as it was given by Richards et al. (2003) and used by Moore et al. (2013) for similar sediment particles.

4.1. Multifrequency Backscatter Inversion (Method 1)

Backscatter is very sensitive to large particles and a change in the PSD width (σ) is expected to be a sensitive factor for a backscatter inversion method such as M1. We tried both options of fixing it prior to the inversion process (case M1.1 of Table 1) and letting it free (case M1.2). In both cases, this inversion method led to largely underestimated SSC outputs (cf. Figure 8a). When letting σ free, inversion outputs were not only biased but also highly scattered. We also tried to adapt Method 1 using the mica-specific model instead of the generic model (case M1.3) without any improvement.

Backscatter-based inversion methods were originally developed and tested on marine sand suspensions. Most often, sand suspensions are well-sorted, that is, they have a narrow PSD with small σ. For this reason, only one parameter has been usually used to describe the particle size, either by considering a single size, or by using a normal or lognormal PSD of fixed σ. For instance, Thorne and Hurther (2014) set $\sigma \approx 0.38$ in their study focused on sand suspensions.

Fine sediments often show a much broader PSD making σ become a critical parameter. This is illustrated in Figure 1b showing s_v values for three PSDs with different widths in blue, orange, and green. A difference in PSD width (σ) leads to a significant difference in backscatter (log-scale). At common ADCP or ABS frequencies, the backscatter response of fine sediments is likely to be located in the deep Rayleigh regime, that is, $ka \ll 1$ where k is the wave number and a the particle radius. In this regime, s_v is proportional to
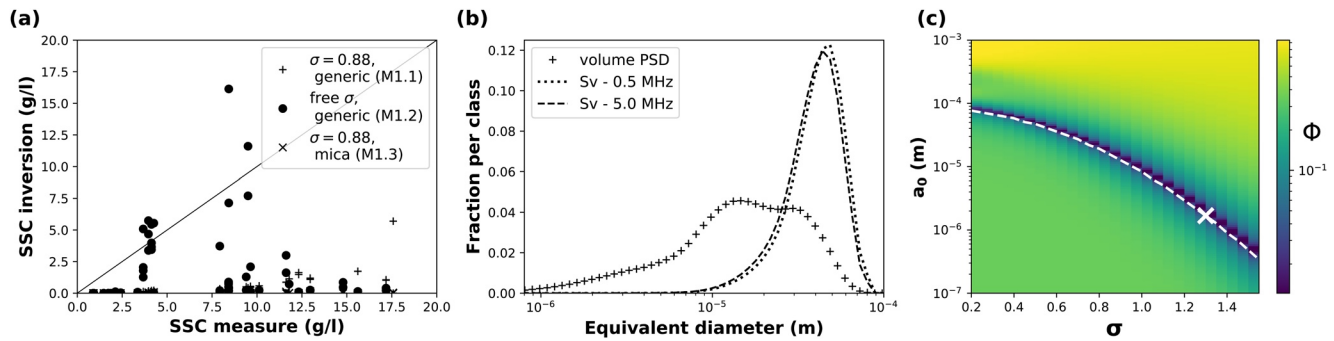
Figure 8. Backscatter multifrequency inversion outputs (Method 1): (a) inverse suspended sediment concentration (SSC) versus measured SSC, in the cases of Particle Size Distribution (PSD) width (σ) fixed prior to the inversion (case M1.1 of Table 1), σ left free in the inversion (case M1.2), using the mica-specific model instead of the generic model (case M1.3). A solid line is perfect agreement line; (b) mean volume PSD measured by laser diffraction (crosses) and contribution to s_v per size class at 0.5 and 5.0 MHz (dashed lines); (c) example of Φ inversion objective function (Equation 6) values in the parameter space (a_0, σ), the white dashed line shows the local minimum valley, the cross indicates the location of the absolute minimum of Φ that is used to retrieve the inverse parameters (SSC, a_0, and σ in this case).

~a^3 (compare blue and pink bars in Figure 1b). Therefore, the right tail of the PSD corresponding to large particles actually contributes much more to the backscatter than the left tail (small particles) does. This is illustrated in Figure 8b that shows a simulation of the fraction of the total s_v due to each particle-size class at 0.5 and 5.0 MHz, compared to the volume PSD measured by laser diffraction. At 5.0 MHz, 80% of the backscatter is produced by particles >30 μm in diameter, although these particles accounts for only ~20% of the total SSC. Then, inversion methods based on backscatter and applied in the deep Rayleigh regime tend to inverse only the right tail of a broad PSD. The inverse PSD is in a way extrapolated from its right tail, making the inversion output very sensitive to any small error in s_v measurement or in the backscatter model itself.

This effect is also illustrated in Figure 8c, showing an example of Φ objective function (Equation 6) values in the parameter space (a_0, σ). One can see that the minimum values of Φ draw a valley (dashed white line) rather than a single well. Therefore, multiple satisfactory solutions might exist. These solutions fit s_v measurements but lead to different inverse SSC, a_0 and σ. The inverse a_0 is less sensitive to σ for narrow PSDs. When σ increases, inverse a_0 becomes more sensitive to σ (see Figure 8c). Then, a small error in fixing σ prior to the inversion may lead to larger errors on inverse a_0 and SSC.

We conclude that efficient particles in terms of backscatter should be present when applying multifrequency inversion methods only based on backscatter such as Method 1. This type of method might not be suitable for suspensions having a broad PSD in the deep Rayleigh regime, which is usually the case for river fine sediments at common ADCP or ABS frequencies.

4.2. Multifrequency Attenuation Inversion (Method 2)

Method 2 SSC inversion outputs were globally underestimated and largely scattered when using the spherical model (Urick, 1948) for viscous attenuation (case M2.1 and M2.2 of Table 1). Moore et al. (2013) made similar observations when inverting the acoustic signal using this model.

The best inversion results were obtained in case M2.3 using Richards et al. (2003) oblate spheroid model for viscous attenuation (α_{sv}) and the mica-specific model of Moate and Thorne (2012) for scattering attenuation (α_{ss}). Both objective functions Γ (Equation 7) and Φ (Equation 6) were tested, results are shown in Figures 9a and 9b, respectively. Differences between Γ and Φ are discussed below. In case M2.3, PSD width (σ) was set to 0.88 and aspect ratio (h) was set to 1/40. Inverted parameters were only SSC and a_0. Mean inverse D_{50} (= $2a_0$) using Γ and Φ objective functions were 20 and 13 μm, respectively. To test the sensitivity of the inversion to σ and h parameters, additional computations were processed for other plausible values of σ and h (0.7 and 1.1, 1/80 and 1/20, respectively, illustrated in Figures 9a and 9b by gray crosses and gray triangles, respectively). We do not observe large variations of inverse SSC when changing σ or h values, except at low concentration using Φ objective function (cf. Figure 9b). In addition to SSC and a_0, we also
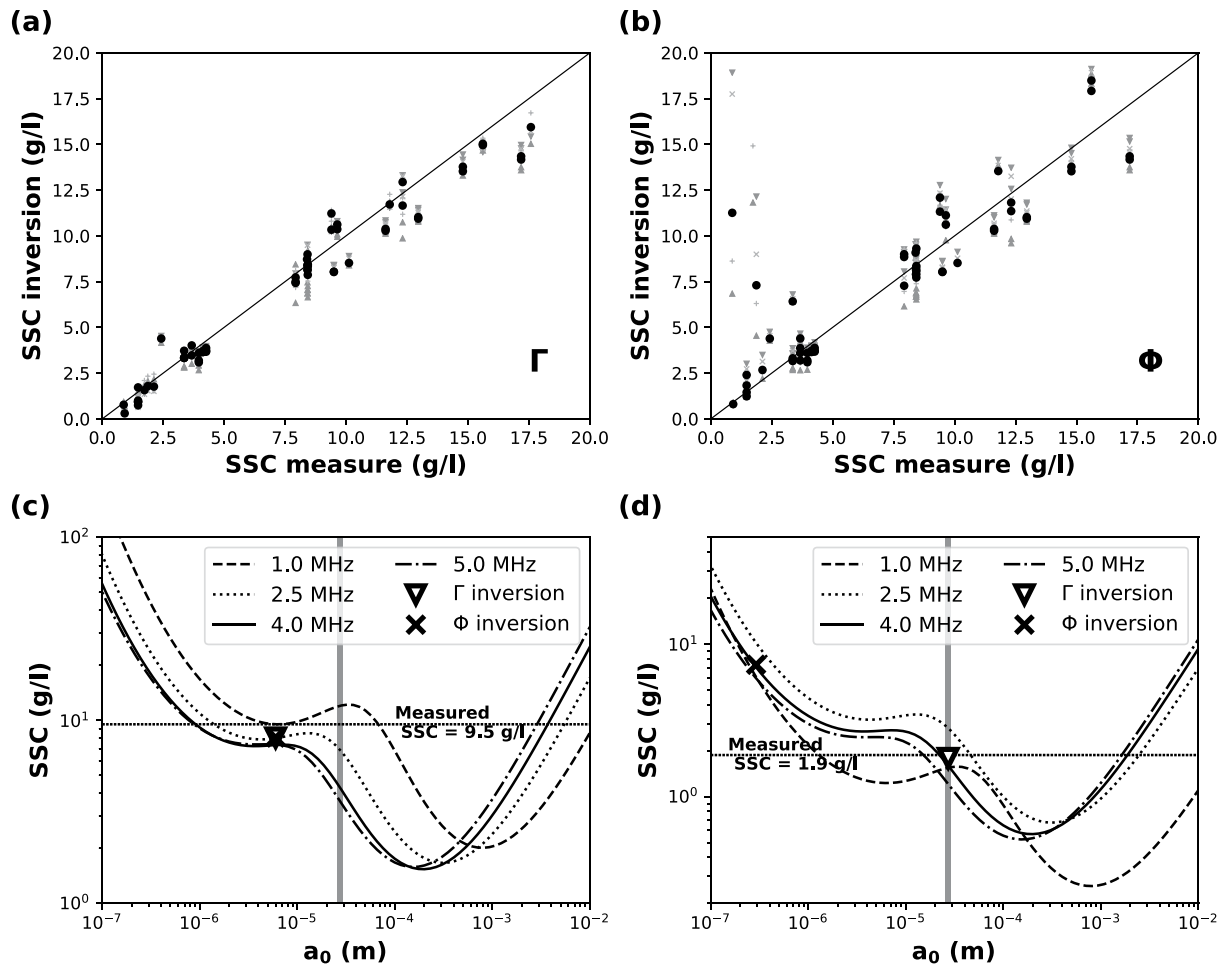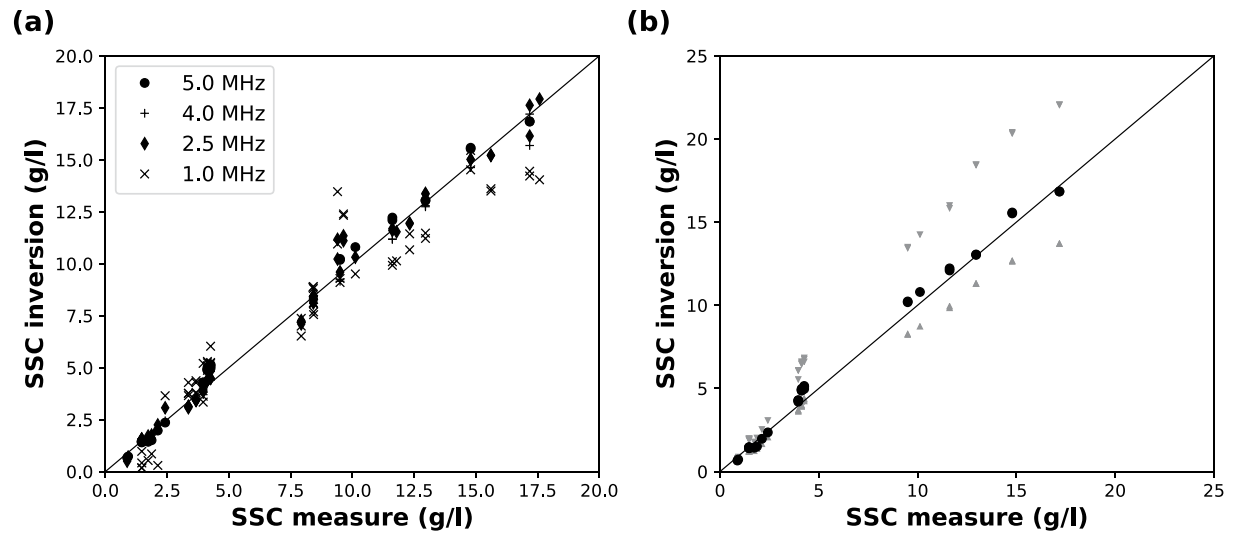
Figure 9. Multifrequency attenuation inversion outputs (Method 2), case M2.3 (cf. Table 1). (a) and (b) Inverse suspended sediment concentration (SSC) versus measured SSC using the Γ objective function (a); using the Φ objective function (b). Black circles show inverse SSC for $\sigma = 0.88$ and $h = 1/40$. Downward and upward gray triangles show inverse SSC for $h = 1/80$ and $h = 1/20$, respectively. Crosses (+) and (×) show inverse SSC for $\sigma = 0.7$ and $\sigma = 1.1$, respectively. The solid line shows perfect agreement. (b) and (c) Examples of SSC modeled from measured acoustic attenuation at various frequencies in case M2.3 (cf. Table 1) versus the median radius (a_0) of the volume lognormal Particle Size Distribution (assumed lognormal) for two different concentrations: (b) SSC = 9.5 g/l; (c) SSC = 1.9 g/l. Horizontal lines show the measured SSC, vertical gray lines show the upper limit set to a_0 in the inversion process, crosses, and triangles show inversion outputs using Φ and Γ objective functions, respectively.

tried to invert σ (case M2.4) or h (case M2.5) but inverted SSC outputs were globally more scattered and less accurate in both cases.

As many inversion methods, Method 2 basically looks for the parameter set for which inverse SSC is the same at all frequencies. This is illustrated graphically for two different concentrations in Figures 9c and 9d (case M2.3 was used for computations). Theoretically, all the curves should meet at one single point, that will provide a_0 and SSC inversion outputs. In practice, the matching point could sometimes be difficult to find. One can observe in Figure 9c that the curves are close to each other in two regions: for a median radius (a_0) corresponding to fine particles (1–10 μm) where viscous attenuation dominates, but also in a region corresponding to sand particles (100–1,000 μm) where scattering attenuation dominates. When applying Method 2 to fine sediments, an upper a_0 limit needs be set to constrain the inversion to the fine sediment region. This limit was set to 30 μm in this study (vertical gray line in Figures 9c and 9d).

The objective functions Γ and Φ are designed to look for the matching point where inverse SSC is similar at all frequencies. Importantly, Φ objective function detects the smallest relative standard deviation between the curves while Γ detects their minimal absolute distance. Objective function Γ is also less sensitive to outliers. For these reasons, Γ will more likely detect a solution in a region where SSC is minimal, that is, close

Figure 10. Single-frequency backscatter and attenuation inversion outputs (Method 3): (a) for the various sonar frequencies, with Particle Size Distribution width (σ) set to 0.88; (b) at 5.0 MHz, inverse suspended sediment concentration for $\sigma = 0.88$ (circles), $\sigma = 0.7$ (downward triangles) and $\sigma = 1.0$ (upward triangles). Solid lines show perfect agreement.

to the peak of viscous attenuation in the region 1–10 μm. This is a bias that led to good inverse SSC outputs in the present study (see Figure 9a) but it will not be necessary the case when applying the method to other type of sediments. Then, the authors recommend the use of Φ objective function to avoid this bias, even if the results are more scattered.

More generally, Figure 9d illustrates the limits of multifrequency inversion techniques based on attenuation only. Compared to backscatter (s_v), α_s increases relatively slowly with frequency (cf. Figure 1d). Precise measurement of α_s is crucial to obtain accurate inverse SSC. When using common ADCP or ABS instruments, only a few frequencies are available, that are relatively low and close to each other. A clear matching point between the curves may be difficult to obtain as illustrated in Figure 9d. The difficulty increases when α_s is low, that is, when SSC is low and/or when using low frequencies. Low α_s may result in higher relative error in α_s measurement leading to unclear matching point and then inaccurate inverse SSC. This is probably the reason why Φ inversion outputs were sometimes very far from the measured values at low concentration (see Figure 9b).

We conclude that Method 2 can produce fairly accurate outputs when using the Richards et al. (2003) oblate spheroid model. One major advantage of this method is that instrument calibration is not required. Two parameters (σ and h) should be determined prior to the inversion but their variation in space and time may not strongly affect the inverse SSC. More important is to obtain a precise measurement of α_s and a clear matching point. This will more likely happen for high concentrations (> 2 g/l) and when using high frequencies (> 1.0 MHz) when frequencies are enough separated.

4.3. Single-Frequency Backscatter and Attenuation Inversion (Method 3)

The Method 3 consists in estimating SSC and median radius (a_0) assuming a lognormal PSD of fixed width (σ), using the ratio of attenuation to backscatter at one single frequency. Figure 10a shows Method 3 inversion results with σ set to 0.88 (case M3 of Table 1). Good agreement was found with SSC measurements, but inversion outputs were more scattered at 1.0 MHz. This is probably due to higher uncertainties in the acoustic measurements, as s_v in particular becomes very small at lower frequencies. The mean D_{50} of the inverse volume PSD varied from 6.9 μm at 5.0 MHz to 10.4 μm at 1.0 MHz. These values are substantially smaller than the value of 14.6 μm obtained by laser diffraction. However, this is consistent with Section 3.2 results: when using the spherical model of Urick (1948) for computing viscous attenuation, particle size twice smaller than the PSD measured by laser diffraction leads to better agreement between acoustic
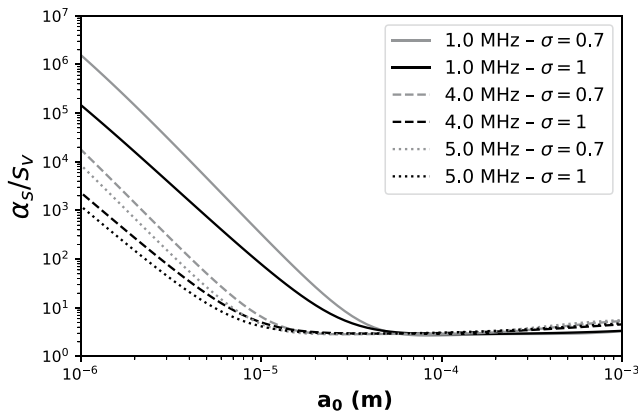
Figure 11. theoretical ratio α_s/s_v as a function of the median radius a_0 of the lognormal volume Particle Size Distribution for $\sigma = 0.7$ and $\sigma = 1.0$ at 1.0, 4.0, and 5.0 MHz.

modeling and measurements. A one third smaller D_{50} was obtained from inversion at the very end of the experiment, when the pumps were turned off, which is consistent with the expected drop in particle size.

This method is obviously sensitive to σ parameter. We performed the inversion for $\sigma = 0.7$ and $\sigma = 1.0$. At 5.0 MHz for instance, if σ varies over 0.7–1.0, inverse SSC vary by $\pm16\%$ (cf. Figure 10b). Interestingly, this relative error is fairly constant with SSC, since the absolute error becomes smaller as SSC decreases.

The cause of the relative success of this method is illustrated in Figure 11 showing α_s/s_v ratio as a function of the median radius (a_0) of the lognormal PSD, for $\sigma = 0.7$ and $\sigma = 1.0$ at 1.0, 4.0, and 5.0 MHz. One can see that α_s/s_v ratio is very sensitive to a_0 for fine sediments. This is due to s_v increasing with size while viscous attenuation decreases, leading to a fast drop of α_s/s_v when the particle size increases in the fine sediment mode. When scattering attenuation starts to become dominant, α_s reaches a local minimum and starts to increase with size. It makes α_s/s_v increasing slowly up to a constant value in the geometric regime ($\alpha_s/s_v \approx 6$).

We deduce from Figure 11 that this inversion method should be applied only when viscous attenuation dominates. It approximately corresponds to $\alpha_s/s_v > 10$. For example, this threshold corresponds to a volume PSD D_{50} of ~50 μm for $\sigma = 0.7$ at 1.0 MHz, and a volume PSD D_{50} of ~10 μm for $\sigma = 1.0$ at 5.0 MHz. Therefore, this inversion method can be suitable, but for silt and clay sediment particles only.

An interesting feature showed in Figure 11 is that the slope of α_s/s_v does not change with frequency, that is, the sensitivity of this method does not depend on frequency. Theoretically, one will prefer using a lower frequency in order to increase the maximum particle size to which the inversion is possible. In practice however, using a lower frequency will make α_s and s_v measurements more uncertain, leading to less precise inversion outputs. The choice of an appropriate frequency might be a trade-off between these two aspects of the problem.

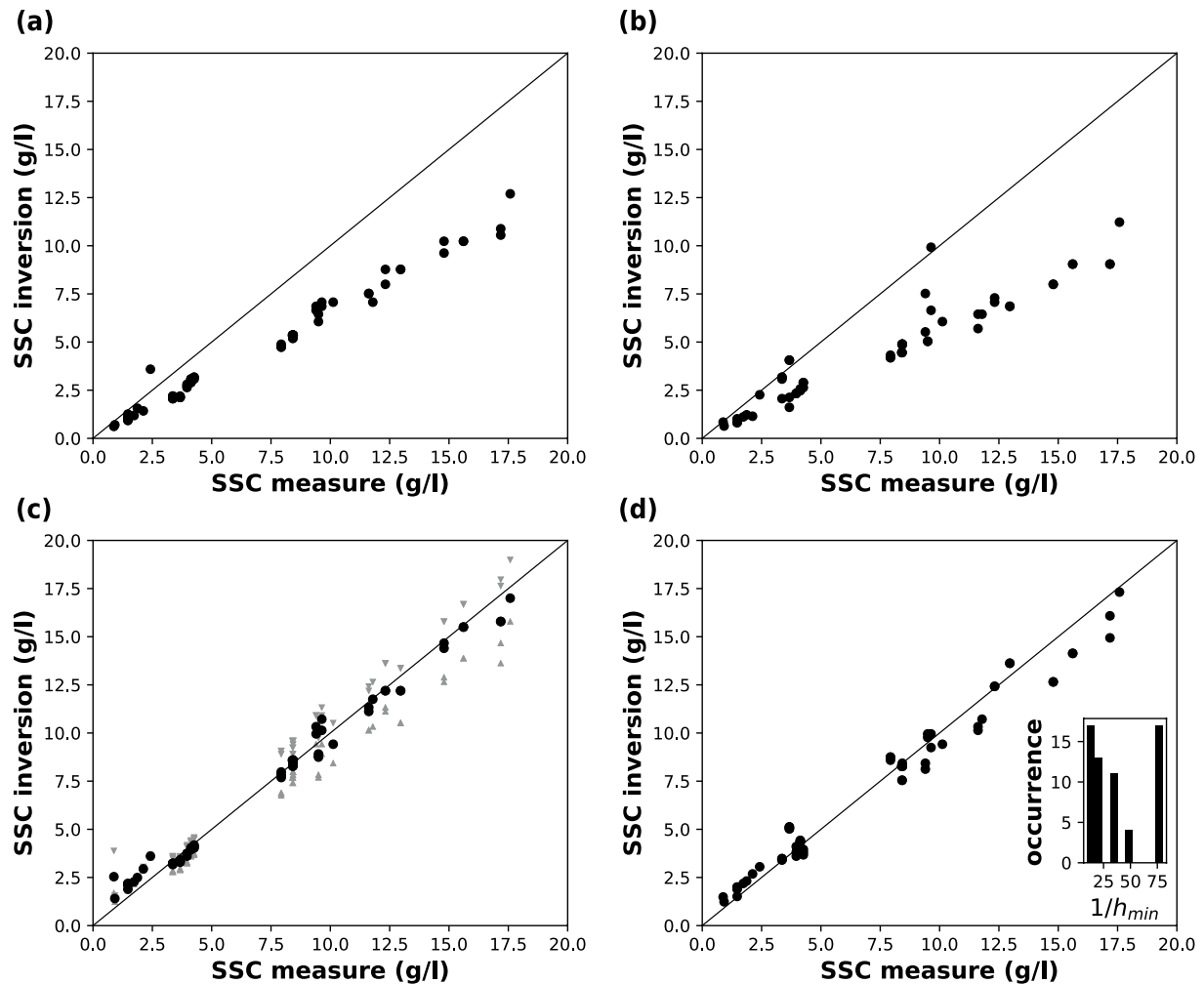### 4.4. Multifrequency Backscatter and Attenuation Inversion (Method 4)

The Method 4 consists in estimating particle parameters (depending on implementation, cf. Table 1) using attenuation and backscatter at several frequencies.

Figure 12a shows Method 4 inverse SSC outputs for case M4.1 (cf. Table 1). One can see that inverse SSC is generally underestimated by ~40%. Then, considering that attenuation is mainly driven by finer particles and backscatter by coarser ones, which should be the case for typical river flows, we tried to give more freedom to the particle size by using a bimodal PSD (case M4.2). However, besides a much longer computational time, the outputs shown in Figure 12b were very similar to case M4.1.

Figure 12c shows case M4.3 inversion outputs. Computing viscous attenuation with Richards et al. (2003) oblate spheroid model and using the mica-specific model for scattering attenuation and backscattering significantly improves the results, with a mean relative error of 13%. This could be expected from Section 3.2 since this model configuration led to the best direct model optimization (see Figures 6e and 6f).

Finally, Figure 12d shows inversion outputs obtained when inverting h_{min} parameter at the same time as a_0, σ and SSC (case M4.4). Inverse SSC values were a little bit underestimated and more scattered at high concentration than when fixing h_{min} prior to the inversion, but the mean relative error remained fairly acceptable around 13%. However, inverse h_{min} values were scattered and close to the bounds of the inversion range which casts doubt on the feasibility of h_{min} inversion.

In both cases M4.3 and M4.4 (Figures 12c and 12d), inverse σ values were often very close to the upper bound of the inversion range that was set to 1.2. When reducing or increasing the σ upper bound from 0.7 to 1.3, inverse σ values remained close to that bound but inverse SSC did not vary substantially. Beyond 1.3,

Figure 12. Multifrequency backscatter and attenuation inversion (Method 4): (a) case M4.1 (cf. Table 1), (Urick, 1948) spherical model, lognormal Particle Size Distribution [PSD]; (b) case M4.2, spherical model, bimodal PSD; (c) case M4.3 (Richards et al., 2003), oblate spheroid model, lognormal PSD, minimum particle aspect ratio (h_{min}) set to 1/40 (black circles). Downward and upward gray triangles show inverse suspended sediment concentration (SSC) range for h of 1/80 and 1/20 respectively; (d) case M4.4, inverting h_{min} in addition to PSD parameters and SSC, the obtained values for h_{min} are represented on a histogram in the bottom right corner. Solid lines show perfect agreement.

inverse SSC outputs tended to be overestimated and more scattered. These relatively high σ values led to a relatively small inverse volume PSD mean D_{50} of 6.4 and 7.4 µm for cases M4.3 and M4.4, respectively. No clear drop in inverse a_0 for measurements taken when the pumps were turned off was observed, contrary to what was expected. The reason why a broader PSD with smaller a_0 better satisfies the inversion optimization process is still unclear.

We conclude that Method 4 can lead to accurate SSC inversion outputs when using the oblate spheroid model. Inverse SSC is still accurate without specifying the value of neither σ nor h_{min} prior to the inversion. However, inverse parameters σ and h_{min} were sometimes unrealistic.

5. Discussion

5.1. Acoustic Modeling Issues

An interesting result of this study is that, even if existing models failed in modeling acoustic parameters α_s and s_v (see Figure 6) when using the PSDs measured by laser diffraction, it was still possible to find an alternative PSD that made these acoustic models work much better. As shown in Section 3, the "optimal" PSDs

found using various model configurations were not drastically different from the laser diffracted PSDs—but always had smaller D_{50}. A similar result was found in Section 4 when testing various inversion methods: the methods based on both backscatter and attenuation (Method 3 and 4) that led to good agreement between measured and inverse SSCs also led to inverse D_{50} smaller than 14.6 µm, the mean D_{50} measured by laser diffraction. For example, optimal D_{50} was 7.3 µm in Section 3, case *ab* (spherical model) whereas inversion method M3, that uses the same model configuration, led to mean inverse D_{50} (over all frequencies) of 8.3 µm. Similarly, optimal D_{50} was also 7.3 µm in case *ef* in Section 3 (oblate spheroids model with variable aspect ratio *h*), not far from mean inverse $D_{50} = 6.4$ µm of method M4.3 that uses the same model configuration.

To the authors, it means that existing acoustic models are suitable for fine natural sediments, but the "acoustic particle radius" parameter (*a*) used in these models does not correspond to the "laser diffracted particle radius" measured by laser diffraction. Acoustic models and laser diffraction measurement rely on strong hypotheses on particle shape. These hypotheses do not have the same implications depending on the physical process that is considered: acoustic scattering, acoustic energy losses due to viscous drag or light diffraction. The "particle radius" parameter may not be the same depending on the process that is considered, except in the ideal case of spherical particles.

Semiempirical acoustic models were successfully developed in marine science for natural sand particles through laboratory experiments. These models allowed to relate a "particle radius" measured by sieving to the acoustic backscatter and attenuation produced by the particles. Similar semiempirical models could be developed for natural fine particles, relating a "particle radius" measured by laser diffraction to backscatter and attenuation. To the authors, such models could definitely improve signal inversion techniques. Ideally, they would take into account the effect of particle density (ρ_s) following the work of Moate and Thorne (2012) as well as the effect of particle flattening (aspect ratio *h* of the present study).

We could wonder whether organic suspended particles might also explain the uncertainties of existing models in rivers (Aleixo et al., 2020) and consider organic content quantification. Nevertheless, it was considered as negligible in this experiment as concentration in sediment particles was high and the ratios of density and compressibility way lower for organic particles.

5.2. Inversion Strategies

In this study, inversion methods M3 and M4 that use both backscatter (s_v) and attenuation (α_s) led to better results than the methods based only on backscatter (M1) or only on attenuation (M2). To the authors, this is due to the fact that, for the case of natural fine sediment suspensions that usually have a wide PSD, α_s is mainly due to the finest particles (left side of the PSD) while s_v is driven by the biggest particles (right side of the PSD, see Figure 8b). Then, α_s and s_v provide different information and better constrain the inversion when used together. Also, using more and higher frequencies improves the inversion efficiency and allows to inverse more parameters (SSC, a_0, σ, and $h_{\min}$ were inverted in case M4.4).

We applied rather arbitrary coefficients in Method 4 to account for the fact that α_s provides more reliable information than s_v, and that higher frequencies provide more reliable information than lower ones. Such coefficients could obviously be improved, for instance by relating them to measured α_s or s_v absolute values or standard deviation. Finally, only one type of sediment was used in this study. Acoustic models and inversion methods presented in this study need to be tested on different sediment suspensions and in the field.

5.3. Field Applications

In this part, we will summarize how the results obtained in this study can be use to analyze field measurements. For now, any SSC acoustic inversion method requires prior information on the suspended particles. All the methods presented in this study apply to homogeneous suspensions. When the suspension is homogeneous along the acoustic beams, an empirical linear relation can be found between SSC and α_s or s_v (see Figure 5). However, these relations are very sensitive to any change in particle characteristics, and particularly to any small evolution of the PSD (see Figure 1). The inversion methods presented in this study are

expected to be less sensitive to the PSD as at least one PSD parameter (median radius a_0) is always inverted. All methods but method M2 require a calibrated instrument, which is necessary to obtain s_v measurements.

If the suspension is purely sand, method M1 may be applicable as it has been developed for marine sand suspensions. This method requires at least two frequencies and a calibrated instrument. If the suspension is purely composed of fines, the authors recommend method M4.3 when several frequencies are available as it was using this method that the results were the most accurate and robust. If only one frequency is available, method M3 may be a good choice. Indeed, it gave better results than method M1. If several frequencies are available but the instrument is not calibrated, try method M2.3. If the suspension is bimodal, that is, composed of a mix of fines and sand, two options could be tested (not implemented in this study): (a) use method M1 to invert sand SSC and method M2 to invert fine SSC, then sum the concentrations; (b) use method M4.3 with a bimodal PSD instead of lognormal; inverting at least SSC, a_1 and a_2. Finally, in the perspective of developing inversion methods suitable for heterogeneous bimodal suspensions commonly found in rivers, it seems to the authors that methods M3 and M4 are still interesting. Usually, fine PSD does not vary very much throughout the river cross section. If one finds a zone where the suspension is homogeneous at least on the first 5 to 10 sonar cells after the transducers, for instance deploying the instrument horizontally near the river bank, method M3 or M4 could then provide an estimate of fine particle characteristics (a_0, and potentially σ and h). These parameters could then be very helpful to constrain the inversion throughout the entire river cross-section. This is interesting all the more since only low frequencies usually have a sufficient detection range to cover the entire river cross-section, which results in less available information and a limited number of parameters that could potentially be inverted.

6. Conclusion

The efficiency of existing acoustic backscatter and attenuation models and inversion methods for fine sediments was evaluated experimentally. We measured the acoustic response of a suspension of fine river particles with diameters ranging from 1 to $100\,\mu$m (D_{50} = 14.6 μm) at various concentrations in a tank from 1 to 18 g/l. The theoretical acoustic response was computed using the suspended sediment concentration (SSC) and particle size distribution (PSD) data from water samples. The agreement between modeled and measured responses was found to be relatively poor, particularly regarding backscatter. However, a simple sensitivity test showed that a PSD finer than the PSD measured by laser diffraction could lead to a much better agreement between models and measurements. This makes it hard to conclude which of the acoustic models or the particle characteristic measurements were wrong. Taking into account the oblate shape of the particles strongly improve the results for attenuation simply considering that the laser diffraction measurement gives the semimajor axis of the spheroids.

River SSC acoustic monitoring would greatly benefit from the development of semiempirical attenuation and backscatter models for fine sediments, as it has been done in marine science for sand particles. Such a model might need to include new input parameters describing the shape of the particles. We showed that developing such kind of models requires well-characterized sediment particles, particularly regarding their size and shape.

While modeling the acoustic response of fine particles is challenging, perfect acoustic models are not always required for efficient signal inversion. In that perspective, four inversion methods were evaluated in this study, in the simplest case of a homogeneous suspension along the acoustic beams. The backscatter-based inversion method (Method 1) led to unrealistic SSC outputs. The attenuation-based method (Method 2) better succeeded in retrieving SSC, when σ (PSD width) and h (particle aspect ratio) values were given prior to the inversion. Indeed, in the deep Rayleigh regime ($ka \ll 1$), sediment attenuation (α_s) provides more information on suspended particles than backscatter. Combining both attenuation and backscatter information is a promising way of improving inversion techniques. Attenuation to the backscatter ratio (Method 3) allowed us to accurately invert SSC using only one frequency, when a proper value of σ was provided prior to the inversion. Using multiple frequencies (Method 4) eventually allowed to accurately retrieve SSC without prior assumption on σ or h. However, this led to unexpectedly high inverse σ values, the source of this problem being still unclear. Obviously, the efficiency of these techniques now needs to be assessed through field experiments.

This work aims to be a step toward river fine sediment monitoring techniques that would rely less on in situ calibration. It claims for the development of multifrequency and calibrated Acoustic Backscatter Systems (ABSs) suitable for river deployment. Using more and higher frequencies would certainly improve α_s and s_v measurement precision, leading to better inversion outputs. Considering measurement uncertainties in the inversion process—for instance using Bayesian inference—also seems to be a promising field of research.

Appendix A: Backscatter and Attenuation Models

A1. Backscatter Models

The volume backscattering coefficient depends on the type and number of scatterers:

$$s_v = \sum_i N_i \sigma_{bs,i} \tag{A1}$$

where N_i (m^{-3}) is the number of scatterers of type i per unit volume and $\sigma_{bs,i}$ (m^2) is their specific backscattering cross-section. For a suspension of solid spherical particles of same radius a (m), material density ρ_s ($\mathrm{kg\,m}^{-3}$) and mass concentration M ($\mathrm{kg\,m}^{-3}$), Equation A1 becomes:

$$\sigma_{bs}(a) = \frac{a^2 f_\infty^2(a)}{4} \qquad N = \frac{3M}{4\pi a^3 \rho_s} \qquad s_v = \frac{3}{16\pi} K^2 M \tag{A2}$$

where f_∞ is the backscattering form factor and $K = f_\infty(a)/\sqrt{a\rho_s}$ describes the backscattering properties of the particles. When considering a PSD rather than a single size, K is computed over the number PSD:

$$K = \left[\frac{\int_0^\infty a^2\, f_\infty^2(a) n(a) da}{\rho_s \int_0^\infty a^3\, n(a) da} \right]^{1/2} \tag{A3}$$

where $n(a)$ is the particle radius probability density function in number of particles (see Section 2.3.2 for conversion procedure between volume and number PSD). For a suspension of natural particles, one generally uses an empirical model to compute the form factor. In this study, we applied the generic semiempirical model proposed by Moate and Thorne (2012):

$$\frac{f_\infty(a)}{\sqrt{\rho_s}} = \frac{(ka)^2 (1 - 0.25 e^{-[(ka-1.5)/0.35]^2})(1 + 0.6 e^{-[(ka-2.9)/1.15]^2})}{42 + 28(ka)^2} \tag{A4}$$

where k ($\mathrm{rad.m}^{-1}$) is the wave number. This formula has been fitted to marine sand particle suspension data.

Moate and Thorne (2012) also fitted a formula more specifically for mica particles, which are plate-like. This mica-specific backscatter model was also be applied for comparison and writes:

$$f_\infty^{mica}(a) = \frac{(ka)^2 (1 - 0.2 e^{-[(ka-1.7)/0.15]^2})(1 + 0.2 e^{-[(ka-3.5)/0.9]^2})}{1.4 + 0.3(ka)^2} \tag{A5}$$

Note that even when using a semiempirical backscatter model (both for the generic or the mica-specific ones), a spherical hypothesis is used to convert sediment mass or volume distribution to number of particles.

A2. Attenuation Models

We used the formula of François and Garrison (1982) to compute α_w from water temperature. Attenuation due to particles can be written as:

$$\alpha_s = \sum_i N_i \frac{\sigma_{e,i}}{2} \tag{A6}$$

where $\sigma_{e,i}$ (m^2) is their total extinction cross-section (Medwin & Clay, 1998). For suspended sediments, the two main sources of energy losses are viscous drag and scattering:

$$\sigma_e = \sigma_{sv} + \sigma_{ss} \tag{A7}$$

where σ_{sv} (m^2) and σ_{ss} (m^2) are the total viscous absorption cross-section and the total scattering cross-section, respectively. For spherical particles of radius a, density ρ_s, and mass concentration M, the attenuation due to suspended particles is:

$$\alpha_s = \frac{3M}{4a\rho_s}(\chi_{sv} + \chi_{ss}) \tag{A8}$$

where $\chi_{sv} = \sigma_{sv}/(2\pi a^2)$ and $\chi_{ss} = \sigma_{ss}/(2\pi a^2)$ are the normalized viscous and scattering total cross-sections, respectively. When considering a PSD rather than a single size, Equation 3 is computed over the entire distribution:

$$\alpha_s = \frac{3M\int_0^\infty a^2(\chi_{sv} + \chi_{ss})n(a)da}{4\rho_s\int_0^\infty a^3 n(a)da} \tag{A9}$$

Note that when the suspension is not homogeneous but varies with range r along the acoustic profile, α_s needs to be integrated over the propagation path.

To estimate the scattering attenuation, we applied the generic semiempirical model of Moate and Thorne (2012):

$$\frac{\chi_{ss}}{\rho_s} = \frac{0.09(ka)^4}{1380 + 560x^2 + 150(ka)^4} \tag{A10}$$

or the mica-specific model:

$$\chi_{ss}^{mica} = \frac{0.30(ka)^4}{1.46 + 0.95x^2 + 0.19(ka)^4} \tag{A11}$$

These equations were derived from the experimental data in a similar way as the Equations A4 and A5 form factor.

One generally estimates viscous attenuation using Urick (1948) formula:

$$
\begin{aligned}
\chi_{sv} &= \frac{2}{3}ka(g-1)^2\left[\frac{s}{s^2 + (g+\delta)^2}\right] \\
g &= \frac{\rho_s}{\rho_0} \quad s = \frac{9}{4\beta a}\left(1 + \frac{1}{\beta a}\right) \quad \delta = \frac{1}{2}\left(1 + \frac{9}{2\beta a}\right) \quad \beta = \sqrt{\frac{\omega}{2\nu_0}}
\end{aligned}
\tag{A12}
$$

where $\rho_0 = 1{,}000$ kg m^{-3}, ω (rad.s^{-1}) is the pulsation and ν_0 is the water kinematic viscosity, set to 0.73×10^{-6} m^2.s^{-1} in this study. Note that this formula was derived from the theory (Hay & Mercer, 1989; Urick, 1948) for the case of spherical particles, but it has been widely applied to natural particles. As far as the authors know, an empirically based viscous attenuation model for natural particles does not exist yet. However, alternative shape models were derived from the theory, for example, for oblate spheroids.

The viscous attenuation coefficient α_{sv} for the case of the oblate spheroid model developed by Richards et al. (2003) is expressed in a similar way as Equation A9 by:

$$\alpha_{sv} = \frac{3M\int_0^\infty a'^2\chi_{sv}(a')n(a')da'}{4\rho_s\int_0^\infty a'^3 n(a')da'} \tag{A13}$$

where a' is the semimajor axis of the spheroid. The total normalized viscous cross-section χ_{sv} is re-written from Urick (1948) (Equation A12), replacing a by a', and s and δ by:

$$
\begin{aligned}
s &= \frac{9}{4\beta ha'}K_{sf}^2\left(1 + \frac{1}{K_{sf}\beta a'}\right) \\
\delta &= L_i + \frac{9}{4\beta ha'}K_{sf}^2
\end{aligned}
\tag{A14}
$$

where L_i is an inertia factor, K_{sf} is a shape factor and $h = b'/a'$ is the ratio between the semiminor and semimajor axis of the spheroid, known as the spheroid aspect ratio. L_i and K_{sf} depend on the orientation of the

spheroid in relation to the oscillatory motion axis. For oblate spheroids oscillating parallel to their axis of symmetry, L_i and K_{sf} are expressed as:

$$
\begin{aligned}
L_{i,\parallel} &= \frac{\alpha_0}{2 - \alpha_0} \qquad \alpha_0 = \frac{2}{\epsilon^2}\left[1 - \sqrt{1 - \epsilon^2}\left(\frac{\sin^{-1}\epsilon}{\epsilon}\right)\right] \\
\epsilon &= \sqrt{1 - h^2} \quad \text{(spheroid eccentricity)} \\
K_{sf,\parallel} &= \frac{8}{3}\left\{\frac{2h}{1 - h^2} + \frac{2(1 - 2h^2)}{(1 - h^2)^{3/2}}\tan^{-1}\left[\frac{(1 - h^2)^{1/2}}{h}\right]\right\}^{-1}
\end{aligned}
\tag{A15}
$$

For oblate spheroids oscillating perpendicularly to their axis of symmetry, L_i and K_{sf} are expressed as:

$$
\begin{aligned}
L_{i,\perp} &= \frac{\gamma_0}{2 - \gamma_0} \qquad \gamma_0 = \frac{\sqrt{1 - \epsilon^2}}{\epsilon^3}\sin^{-1}\epsilon - \left[\frac{1 - \epsilon^2}{\epsilon^2}\right] \\
K_{sf,\perp} &= \frac{8}{3}\left\{-\frac{h}{1 - h^2} - \frac{2h^2 - 3}{(1 - h^2)^{3/2}}\sin^{-1}(1 - h^2)^{1/2}\right\}^{-1}
\end{aligned}
\tag{A16}
$$

Richards et al. (2003) made the assumption of a random orientation of the particles and considered that two-third of the particles have their semimajor axis perpendicular to the direction of sound propagation, and one-third have their semimajor axis parallel to this direction. Thus:

$$
\chi_{sv}(a') = \frac{2}{3}\chi_{sv,\perp}(a') + \frac{1}{3}\chi_{sv,\parallel}(a')
\tag{A17}
$$

where $\chi_{sv,\perp}$ and $\chi_{sv,\parallel}$ are the total normalized viscous cross-sections computed in the case of perpendicular and parallel orientation of the oblate spheroid in relation to the direction of sound propagation, respectively.

Data Availability Statement

Data are available on zenodo (https://doi.org/10.5281/zenodo.5094304).

References

Agrawal, Y. C., & Hanes, D. M. (2015). The implications of laser-diffraction measurements of sediment size distributions in a river to the potential use of acoustic backscatter for sediment measurements. *Water Resources Research*, *51*, 8854–8867. https://doi.org/10.1002/2015wr017268

Aleixo, R., Guerrero, M., Nones, M., & Ruther, N. (2020). Applying ADCPs for long-term monitoring of SSC in rivers. *Water Resources Research*, *56*. https://doi.org/10.1029/2019wr026087

Armijos, E., Crave, A., Espinoza, R., Fraizy, P., Dos Santos, A. L. M. R., Sampaio, F., et al. (2017). Measuring and modeling vertical gradients in suspended sediments in the Solimões/Amazon River. *Hydrological Processes*, *31*, 654–667. https://doi.org/10.1002/hyp.11059

Betteridge, K. F. E., Thorne, P. D., & Cook, R. D. (2008). Calibrating multi-frequency acoustic backscatter systems for studying near-bed suspended sediment transport processes. *Continental Shelf Research*, *28*, 227–235. https://doi.org/10.1016/j.csr.2007.07.007

Burban, P.-Y., Lick, W., & Lick, J. (1989). The flocculation of fine-grained sediments in estuarine waters. *Journal of Geophysical Research*, *94*, 8323–8330. https://doi.org/10.1029/jc094ic06p08323

Downing, A., Thorne, P. D., & Vincent, C. E. (1995). Backscattering from a suspension in the near field of a piston transducer. *Journal of the Acoustical Society of America*, *97*, 1614–1620. https://doi.org/10.1121/1.412100

Dramais, G. (2020). *Observation et modélisation des flux de sable dans les grands cours d'eau* (Theses, Université de Lyon). Retrieved from https://tel.archives-ouvertes.fr/tel-03188258

Droppo, I. G. (2001). Rethinking what constitutes suspended sediment. *Hydrological Processes*, *15*, 1551–1564. https://doi.org/10.1002/hyp.228

Erdoğan, S., Garboczi, E. J., & Fowler, D. (2007). Shape and size of microfine aggregates: X-ray microcomputed tomography vs. laser diffraction. *Powder Technology*, *177*(2), 53–63.

Eshel, G., Levy, G. J., Mingelgrin, U., & Singer, M. J. (2004). Critical evaluation of the use of laser diffraction for particle-size distribution analysis. *Soil Science Society of America Journal*, *68*, 763–743. https://doi.org/10.2136/sssaj2004.0736

François, R. E., & Garrison, G. R. (1982). Sound absorption based on ocean measurements: Part I: Pure water and magnesium sulfate contributions. *Journal of the Acoustical Society of America*, *75*, 896–907. https://doi.org/10.1121/1.388170

Gordon, J., Newland, C., & Gagliardi, S. (2000). *Laboratory performance in the sediment laboratory quality-assurance project, 1996-98* (Vol. 99). US Department of the Interior, US Geological Survey.

Gostiaux, L., & van Haren, H. (2010). Extracting meaningful information from uncalibrated backscattered echo intensity data. *Journal of Atmospheric and Oceanic Technology*, *27*, 943–949. https://doi.org/10.1175/2009jtecho704.1

Gray, J. R., & Gartner, J. W. (2009). Technological advances in suspended-sediment surrogate monitoring. *Water Resources Research*, *45*, W00D29. https://doi.org/10.1029/2008wr007063

Guerrero, M., & Di Federico, V. (2018). Suspended sediment assessment by combining sound attenuation and backscatter measurements—Analytical method and experimental validation. *Advances in Water Resources*, *113*, 167–179. https://doi.org/10.1016/j.advwatres.2018.01.020

Hanes, D. M. (2012). On the possibility of single-frequency acoustic measurement of sand and clay concentrations in uniform suspensions. *Continental Shelf Research*, *46*, 64–66. https://doi.org/10.1016/j.csr.2011.10.008

Haught, D., Venditti, J. G., & Wright, S. A. (2017). Calculation of in situ acoustic sediment attenuation using off-the-shelf horizontal ADCPs in low concentration settings. *Water Resources Research*, *53*, 5017–5037. https://doi.org/10.1002/2016wr019695

Hay, A. E. (1991). Sound scattering from a particle-laden, turbulent jet. *Journal of the Acoustical Society of America*, *90*, 2055–2074. https://doi.org/10.1121/1.401633

Hay, A. E., & Mercer, D. G. (1989). A note on the viscous attenuation of sound in suspensions. *Journal of the Acoustical Society of America*, *85*, 2215–2216. https://doi.org/10.1121/1.397870

Hay, A. E., & Sheng, J. (1992). Vertical profiles of suspended sand concentration and size from multifrequency acoustic backscatter. *Journal of Geophysical Research*, *97*, 15661–15677. https://doi.org/10.1029/92jc01240

Hunter, T. N., Darlison, L., Peakall, J., & Biggs, S. (2012). Using a multi-frequency acoustic backscatter system as an in situ high concentration dispersion monitor. *Chemical Engineering Science*, *80*, 409–418. https://doi.org/10.1016/j.ces.2012.06.038

Hurther, D., Thorne, P. D., Bricault, M., Lemmin, U., & Barnoud, J.-M. (2011). A multi-frequency Acoustic Concentration and Velocity Profiler (ACVP) for boundary layer measurements of fine-scale flow and sediment transport processes. *Coastal Engineering Journal*, *58*, 594–605. https://doi.org/10.1016/j.coastaleng.2011.01.006

Landers, M. N., Straub, T. D., Wood, M. S., & Domanski, M. M. (2016). Sediment acoustic index method for computing continuous suspended-sediment concentrations. In *USGS techniques and methods, book 3, chap. C5.* https://doi.org/10.3133/tm3C5

MacDonald, I. T., Vincent, C. E., Thorne, P. D., & Moate, B. D. (2013). Acoustic scattering from a suspension of flocculated sediments. *Journal of Geophysical Research*, *118*, 2581–2594. https://doi.org/10.1002/jgrc.20197

Masson, M., Angot, H., Le Boscond, C., Launay, M., Dabrin, A., Miège, C., et al. (2018). Sampling of suspended particulate matter using particle traps in the Rhône River: Relevance and representativeness for the monitoring of contaminants. *The Science of the Total Environment*, *637–638*, 538–549. https://doi.org/10.1016/j.scitotenv.2018.04.343

Medwin, H., & Clay, C. S. (1998). *Fundamentals of acoustical oceanography*. Academic Press.

Moate, B. D., & Thorne, P. D. (2012). Interpreting acoustic backscatter from suspended sediments of different and mixed mineralogical composition. *Continental Shelf Research*, *46*, 67–82. https://doi.org/10.1016/j.csr.2011.10.007

Moore, S. A., Le Coz, J., Hurther, D., & Paquier, A. (2012). On the application of horizontal ADCPs to suspended sediment transport surveys in rivers. *Continental Shelf Research*, *46*, 50–63. https://doi.org/10.1016/j.csr.2011.10.013

Moore, S. A., Le Coz, J., Paquier, A., & Hurther, D. (2013). Using multi-frequency acoustic attenuation to monitor grain size and concentration of suspended sediment in rivers. *Journal of the Acoustical Society of America*, *133*, 1959–1970. https://doi.org/10.1121/1.4792645

Orwin, J., & Smart, C. (2004). Short-term spatial and temporal patterns of suspended sediment transfer in proglacial channels, small river glacier, Canada. *Hydrological Processes*, *18*(9), 1521–1542. https://doi.org/10.1002/hyp.1402

Rice, H. P., Fairweather, M., Hunter, T. N., Mahmoud, B., Biggs, S., & Peakall, J. (2014). Measuring particle concentration in multiphase pipe flow using acoustic backscatter: Generalization of the dual-frequency inversion method. *Journal of the Acoustical Society of America*, *136*, 156–169. https://doi.org/10.1121/1.4883376

Richards, S. D., Leighton, T. G., & Brown, N. R. (2003). Visco-inertial absorption in dilute suspensions of irregular particles. *Proceedings of the Royal Society of London*, *459*, 2153–2167. https://doi.org/10.1098/rspa.2003.1126

Rouhnia, M., Keyvani, A., & Strom, K. (2014). Do changes in the size of mud flocs affect the acoustic backscatter values recorded by a Vector ADV? *Continental Shelf Research*, *84*, 84–92. https://doi.org/10.1016/j.csr.2014.05.015

Schaafsma, A. S., & Hay, A. E. (1997). Attenuation in suspensions of irregularly shaped sediment particles: A two-parameter equivalent spherical scatter model. *Journal of the Acoustical Society of America*, *102*, 1485–1502. https://doi.org/10.1121/1.420063

Schjønning, P., McBride, R. A., Keller, T., & Obour, P. B. (2017). Predicting soil particle density from clay and soil organic matter contents. *Geoderma*, *286*, 83–87.

Sheng, J., & Hay, A. E. (1988). An examination of the spherical scatterer approximation in aqueous suspensions of sand. *Journal of the Acoustical Society of America*, *83*, 598–610. https://doi.org/10.1121/1.396153

Sung, C. C., Huang, Y. J., Lai, J. S., & Hwang, G. W. (2008). Ultrasonic measurement of suspended sediment concentrations: An experimental validation of the approach using kaolin suspensions and reservoir sediments under variable thermal conditions. *Hydrological Processes*, *22*, 3149–3154. https://doi.org/10.1002/hyp.6899

Szupiany, R., Lopez Weibel, C., Guerrero, M., Latosinski, F., Wood, M., Dominguez Ruben, L., & Oberg, K. (2019). Estimating sand concentrations using ADCP-based acoustic inversion in a large fluvial system characterized by bi-modal suspended-sediment distributions. *Earth Surface Processes and Landforms*, *44*, 1295–1308. https://doi.org/10.1002/esp.4572

Thomas, L. P., & Marino, B. M. (2021). Empirical approach using Acoustic Doppler Current Profilers for determining particle size distributions in estuaries with highly concentrated suspended matter. *Journal of Hydraulic Engineering*, *147*(7), 04021022. https://doi.org/10.1061/(asce)hy.1943-7900.0001893

Thorne, P. D., & Buckingham, M. J. (2004). Measurements of scattering by suspensions of irregularly shaped sand particles and comparison with a single parameter modified sphere model. *Journal of the Acoustical Society of America*, *116*, 2876–2889. https://doi.org/10.1121/1.1808458

Thorne, P. D., & Hanes, D. M. (2002). A review of acoustic measurement of small-scale sediment processes. *Continental Shelf Research*, *22*, 603–632. https://doi.org/10.1016/s0278-4343(01)00101-7

Thorne, P. D., Hardcastle, P. J., & Soulsby, R. L. (1993). Analysis of acoustic measurements of suspended sediments. *Journal of Geophysical Research*, *98*, 899–910. https://doi.org/10.1029/92jc01855

Thorne, P. D., & Hurther, D. (2014). An overview on the use of backscattered sound for measuring suspended particle size and concentration profiles in non-cohesive inorganic sediment transport studies. *Continental Shelf Research*, *73*, 97–118. https://doi.org/10.1016/j.csr.2013.10.017

Thorne, P. D., Hurther, D., & Moate, B. D. (2011). Acoustic inversions for measuring boundary layer suspended sediment processes. *Journal of the Acoustical Society of America*, *130*, 1188–1200. https://doi.org/10.1121/1.3618728

Thorne, P. D., MacDonald, I. T., & Vincent, C. E. (2014). Modeling acoustic scattering by suspended flocculating sediments. *Continental Shelf Research*, *88*, 81–91. https://doi.org/10.1016/j.csr.2014.07.003

Thorne, P. D., & Meral, R. (2008). Formulations for the scattering properties of suspended sandy sediments for use in the application of acoustics to sediment transport processes. *Continental Shelf Research*, *28*, 309–317. https://doi.org/10.1016/j.csr.2007.08.002

Thosteson, E. D., & Hanes, D. M. (1998). A simplified method for determining sediment size and concentration from multiple frequency acoustic backscatter measurements. *Journal of the Acoustical Society of America*, *104*, 820–830. https://doi.org/10.1121/1.423356

Topping, D. J., & Wright, S. A. (2016). *Long-term continuous acoustical suspended-sediment measurements in rivers—Theory, application, bias, and error*. (USGS Professional Paper 1823). https://doi.org/10.3133/pp1823

Topping, D. J., Wright, S. A., Melis, T. S., & Rubin, D. M. (2007). High-resolution measurements of suspended-sediment concentration and grain size in the Colorado River in Grand Canyon using a multi-frequency acoustic system. In *Proceedings of the 10th international symposium on river sedimentation*.

Urick, R. J. (1948). The absorption of sound in suspensions of irregular particles. *Journal of the Acoustical Society of America*, *20*, 283–289. https://doi.org/10.1121/1.1906373

Venditti, J. G., Church, M., Attard, M. E., & Haught, D. (2016). Use of ADCPs for suspended sediment transport monitoring: An empirical approach. *Water Resources Research*, *52*, 2715–2736. https://doi.org/10.1002/2015wr017348

Vergne, A., Le Coz, J., Berni, C., & Pierrefeu, G. (2020). Using a down-looking multifrequency ABS for measuring suspended sediments in rivers. *Water Resources Research*, *56*(2). https://doi.org/10.1029/2019wr024877

Vincent, C. E., & MacDonald, I. T. (2015). A flocculi model for the acoustic scattering from flocs. *Continental Shelf Research*, *104*, 15–24. https://doi.org/10.1016/j.csr.2015.05.002

Wilson, G. W., & Hay, A. E. (2015). Acoustic backscatter inversion for suspended sediment concentration and size: A new approach using statistical inverse theory. *Continental Shelf Research*, *106*, 130–139. https://doi.org/10.1016/j.csr.2015.07.005

Wright, S. A., Topping, D. J., & Williams, C. A. (2010). Discriminating silt-and-clay from suspended-sand in rivers using side-looking acoustic profilers. In *Proceedings of the 2nd Joint Federal Interagency Sedimentation Conference*.